Applied Mathematics and Computation, Volume 336, November 2018, pp. 368-393
DOI: https://doi.org/10.1016/j.amc.2018.04.076

Low-Mach Number Treatment for Finite-Volume Schemes on Unstructured Meshes

Nicholas Simmonds[a], Panagiotis Tsoutsanis[a,*], Antonis F. Antoniadis[a], Karl W. Jenkins[a], Adrian Gaylard[b]

[a] *Centre for Computational Engineering Sciences, Cranfield University, Cranfield MK43 0AL, United Kingdom*
[b] *Jaguar Land Rover, Banbury Road, Gaydon, Warwick, CV35 0RR, United Kingdom*

Abstract

The paper presents a low-Mach number (LM) treatment technique for high-order, Finite-Volume (FV) schemes for the Euler and the compressible Navier-Stokes equations. We concentrate our efforts on the implementation of the LM treatment for the unstructured mesh framework, both in two and three spatial dimensions, and highlight the key differences compared with the method for structured grids. The main scope of the LM technique is to at least maintain the accuracy of low speed regions without introducing artefacts and hampering the global solution and stability of the numerical scheme. Two families of spatial schemes are considered within the k-exact FV framework: the Monotonic Upstream-Centered Scheme for Conservation Laws (MUSCL) and the Weighted Essentially Non-Oscillatory (WENO). The simulations are advanced in time with an explicit third-order Strong Stability Preserving (SSP) Runge-Kutta method. Several flow problems are considered for inviscid and turbulent flows where the obtained solutions are compared with referenced data. The associated benefits of the method are analysed in terms of overall accuracy, dissipation characteristics, order of scheme, spatial resolution and grid composition.

1. Introduction

One of the most challenging parts of high-resolution numerical schemes is that they have to maintain adaptivity throughout the solution. Adaptivity, in the sense of identifying regions of sharp gradients, often encountered in compressible flows as well as preventing or eliminating any spurious oscillations that can occur; but at the same time they should be adaptive and achieve high-order of accuracy in smooth regions of the flow. There is a delicate balance between the two requirements and is dependent upon the spatial discretisation method, the shock-capturing algorithms, the grid types, the Riemann solvers, the time-stepping algorithms and the integration quadrature rules to name a few.

The numerical methods for unstructured grids have matured and numerous elegant approaches [1–14] and algorithms have been developed in the FV framework for a wide range of applications in Computational Fluid Dynamics. Other state-of-the-art approaches have been developed, such as the Discontinuous Galerkin (DG) [2, 11, 15–18], Spectral Finite-Volume (SFV) methods [12, 19–23], Flux Reconstruction (FR) methods[14, 24] that have been successfully applied for various flow problems. For the FV framework, the first class of high-resolution methods developed for unstructured grids included the Essentially Non-Oscillatory (ENO) type schemes [25, 26], followed by the WENO type schemes [27–30]. In the WENO case, the high-order accuracy was achieved by non-linearly combining a series of high-order reconstruction polynomials arising from a series of reconstruction stencils. Recently, a class of WENO type methods [8, 9] has been successfully extended to hybrid unstructured meshes with various geometrical shapes such as tetrahedrals, hexahedrals, prisms,and

*Corresponding author
Email addresses: n.simmonds@cranfield.ac.uk (Nicholas Simmonds), panagiotis.tsoutsanis@cranfield.ac.uk (Panagiotis Tsoutsanis), a.f.antoniadis@cranfield.ac.uk (Antonis F. Antoniadis), k.w.jenkins@cranfield.ac.uk (Karl W. Jenkins), agaylar1@jaguarlandrover.com (Adrian Gaylard)

pyramids. WENO schemes can achieve very high-order of spatial accuracy across interfaces between cells of different types, and non-oscillatory profiles are produced for discontinuous solutions. This provides greater flexibility to handle complex geometrical shapes in an efficient and accurate manner.

For the majority of the FV numerical methods applied to compressible flows, the dissipation characteristics are proportional to the speed of sound, therefore the low Mach number features are damped by the numerical scheme as noted by Thornber et al. [31]. This is particular important at regions of the flow where the local Mach number is small such in the vicinity of the boundary layer and in vortices arising from shear layers.

There is a wealth of different approaches aiming to improve the dissipation characteristics of numerical methods for compressible flow equations, either by enabling their deployment for very low Mach number flows, or improving their resolution at low Mach number regions [32–42]. In the novel approach of Rieper [41,42], it was shown through an one-dimensional analysis that the right amount of artificial viscosity on each individual characteristic variable is a prerequisite for an upwind scheme to approximate low Mach number flows correctly. A low diffusion preconditioning scheme was developed by Shen et al. [40] using 5^{th}-order WENO scheme, and significant benefits in terms of accuracy and efficiency were noted for low-Mach number flows, as well transonic and supersonic flows.

A thorough analysis of various Roe Riemann solver [43] modifications for low Mach number flows was performed by Li et al. [38], highlighting the dependence on the order of the coefficient of the velocity difference term and pressure difference term, along with some rules for constructing numerical schemes for all-speed flows. A low-dissipation version of Roe Riemann solver [43] was introduced by Oßwald et al. [39] and compared with the approach of Thornber et al. [31]; the former was modifying only the dissipation term in the numerical flux function, in contrast to the approach of Thornber et al.[31], where the evaluation of the physical fluxes is modified. The latter approach exhibited superior behaviour for the Decaying Isotropic Turbulence (DIT) test problem. Additionally, a non-physical high dissipation of energy was noted when using a tetrahedral mesh for the same test case with a second-order FV scheme. Another novel approach of Qu et al. [33] entailed the development of a new Roe-type scheme labelled RoeMAS, that exhibited high-resolution for low Mach number flows as well as robustness against odd-even decoupling.

The work of Nogueira et al. [32], presents the application of a Moving Least Squares (MLS) FV formulation, in conjunction with a low-Mach number fix and a slope limiter. Grid dependency of the schemes was assessed, demonstrating that even high-order schemes can benefit from the low-Mach number fix of Rieper et al. [41,42]. It was highlighted that the accuracy problem of FV schemes for low Mach number flows can be alleviated by using high-order discretisation schemes. The Discontinuous Galerkin (DG) schemes exhibit a similar accuracy problem to the FV schemes as shown by Bassi et al. [44], where it is shown that preconditioning improves accuracy and efficiency of DG schemes in the low Mach number regime.

All of the aforementioned approaches generally involve structured grids, or quadrilateral dominant meshes in 2D. Another new aspect, that was presented by Rieper et al. [45], is that low Mach number accuracy of FV schemes is dependent on the cell geometry, since when applied on a triangular grid, the accuracy problem disappears. A comprehensive asymptotic analysis of this interesting phenomenon for the first-order Roe scheme [43] revealed that the leading-order velocity component normal to a cell edge does not jump, and that the arbitrary orientation of these triangular cells leaves enough degrees of freedom for the velocity field to represent a physical flow. This study did not include higher-order schemes for triangular meshes. However, the second-order Roe scheme [43] on unstructured triangular grids led to completely wrong results. It was assumed that the reconstruction process prevents the establishment of a continuous normal velocity component introducing the inaccurate pressure field. For higher-order schemes a smoother reconstruction which seems to prevent the jumps of the normal velocity component and with it the accuracy problem was identified.

The work in this paper is a revision of the approach of Thornber et al. [31], since the original implementation of the method as it will be demonstrated can not be extended to unstructured grids. A similar approach is introduced by Oßwald et al. [39], where the Roe Riemann solver was employed, however that study employed these schemes to second-order accurate FV schemes only for tetrahedral meshes. Additionally, it was noticed that extra dissipation was observed over the higher wave number range for the DIT test problem, which was not fully understood. To the best of the authors knowledge this is a first attempt to

evaluate the characteristics and the performance of a low-Mach number fix using FV methods for unstructured meshes of various element types for 2D and 3D inviscid and turbulent compressible flows, while also utilising higher-order schemes. In addition, the challenges associated with the modifications are assessed and guidelines are provided for further development of these techniques. The compactness of the proposed scheme following the philosophy of Thornber et al. [31] can be utilised with any Riemann solver in order to remove the Mach number dependence, and improve the resolution at low Mach number regions of the flow. The original LM treatment proposed by Thornber et al. [31] is not directly transferable to any grid-type since different mesh elements have different dissipation characteristics, therefore a unified treatment is implemented that is suitable for all element types and through the computational results obtained the difference between the original treatment, and the modified one are presented. Finally, a desirable feature of this treatment is the efficient implementation in any compressible code, for any numerical scheme that uses a Riemann solver with negligible additional computational expense.

The rest of the paper is organized as follows: section 2 is dedicated to the description of the numerical framework, including the spatial disretisation, MUSCL, WENO reconstruction techniques, the proposed low-Mach number treatment, fluxes approximation and the time-stepping algorithm. In Section 3 the numerical results obtained for various schemes and LM treatments including the inviscid subsonic flow past a 2D circular cylinder, the inviscid supersonic flow past a 2D circular cylinder, the inviscid 2D vortex evolution, the inviscid 3D Taylor Green Vortex and the turbulent flow around the 3D SD7003 airfoil are presented. Finally, the conclusions of the present study are outlined in the last section.

2. General Formulation

The compressible Navier-Stokes equations are considered, written in conservative form as:

$$\frac{\partial \mathbf{U}(\mathbf{x},t)}{\partial t} + \nabla(\mathbf{F_c}(\mathbf{U}) - \mathbf{F_v}(\mathbf{U}, \nabla\mathbf{U})) = 0, \tag{1}$$

where $\mathbf{U}$ is the vector of the conserved mean flow variables, and $\mathbf{F_c}$ and $\mathbf{F_v}$ are the inviscid and viscous flux vectors, respectively:

$$\begin{aligned}
\mathbf{U} &= [\rho, \rho u, \rho v, \rho w, E]^T, \\
F_c^{\mathbf{x}} &= \left[\rho u, \rho u^2 + p, \rho uv, \rho uw, u(E+p)\right]^T, \\
F_c^{\mathbf{y}} &= \left[\rho v, \rho uv, \rho v^2 + p, \rho vw, v(E+p),\right]^T, \\
F_c^{\mathbf{z}} &= \left[\rho w, \rho uw, \rho vw, \rho w^2 + p, w(E+p)\right]^T, \\
F_v^{\mathbf{x}} &= [0, \tau_{xx}, \tau_{xy}, \tau_{xz}, \Theta_x]^T, \\
F_v^{\mathbf{y}} &= [0, \tau_{xy}, \tau_{yy}, \tau_{yz}, \Theta_y]^T, \\
F_v^{\mathbf{z}} &= [0, \tau_{xz}, \tau_{yz}, \tau_{zz}, \Theta_z]^T.
\end{aligned} \tag{2}$$

In the above equations, ρ is the density; u, v, w are the velocity components in x, y and z Cartesian coordinates, respectively. Calorically perfect gas is assumed where the total energy per unit volume is calculated by $E = p/(\gamma - 1) + (1/2)\rho(u^2 + v^2 + w^2)$, where p is the pressure, $\gamma = 1.4$ is the ratio of specific heats for air at normal atmospheric conditions; The laminar viscosity is related to the temperature through the Sutherland law:

$$\frac{\mu_l}{\mu_0} = \left(\frac{T}{T_0}\right)^{\frac{3}{2}} \frac{T_0 + S}{T + S}, \tag{3}$$

S is the Sutherland temperature and the subscript 0 denotes a reference state for the corresponding variables. Unless otherwise stated, the reference values are taken at atmospheric conditions (sea level): dynamic viscosity $\mu_0 = 1.7894 \times 10^{-5} kg/(ms)$; reference temperatures $T_0 = 288.16K$; $S = 110.4K$; and Prandtl

number $Pr = 0.72$. The approximation of the viscous stress tensor τ_{ij} is defined by:

$$\tau_{ij} = \mu_l \left(\frac{\partial \mathbf{u}_i}{\partial \mathbf{x}_j} + \frac{\partial \mathbf{u}_j}{\partial \mathbf{x}_i} - \frac{2}{3} \frac{\partial \mathbf{u}_k}{\partial \mathbf{x}_k} \delta_{ij} \right), \tag{4}$$

where δ_{ij} is the Kronecker delta and the subscripts i, j, k refer to the Cartesian coordinate components $\mathbf{x} = (x, y, z)$. The work of viscous stresses and heat conduction, Θ, is given by:

$$\begin{aligned}
\Theta_x &= u\tau_{xx} + v\tau_{xy} + w\tau_{xz} + \left(\frac{\mu_l}{Pr}\right) \frac{\gamma}{(\gamma - 1)} \frac{\partial T}{\partial x}, \\
\Theta_y &= u\tau_{yx} + v\tau_{yy} + w\tau_{yz} + \left(\frac{\mu_l}{Pr}\right) \frac{\gamma}{(\gamma - 1)} \frac{\partial T}{\partial y}, \\
\Theta_z &= u\tau_{zz} + v\tau_{zy} + w\tau_{zz} + \left(\frac{\mu_l}{Pr}\right) \frac{\gamma}{(\gamma - 1)} \frac{\partial T}{\partial z}.
\end{aligned} \tag{5}$$

2.1. High-order finite-volume k-exact least square reconstruction

The discretisation in a domain Ω is achieved by combining conforming arbitrary shaped elements of volume $|V_i|$. Integrating Eq. (1) over a mesh element using the finite-volume formulation the following ordinary differential equation is obtained:

$$\begin{aligned}
\frac{d\mathbf{U}_i}{dt} = &- \frac{1}{|V_i|} \sum_{l=1}^{N_f} \sum_{\alpha=1}^{N_{qp}} \mathbf{F}_c^{\mathbf{n},\mathbf{l}} \left(\mathbf{U}(\mathbf{x}_\alpha, t) \right) \omega_\alpha |A_l| \\
&+ \frac{1}{|V_i|} \sum_{l=1}^{N_f} \sum_{\alpha=1}^{N_{qp}} \mathbf{F}_v^{\mathbf{n},\mathbf{l}} \left(\mathbf{U}(\mathbf{x}_\alpha, t), \nabla \mathbf{U}(\mathbf{x}_\alpha, t) \right) \omega_\alpha |A_l|,
\end{aligned} \tag{6}$$

where $\mathbf{U}_i$ is the volume averaged conserved variable vector, N_f is the number of faces per element, N_{qp} is the number of quadrature points used for approximating the surface integrals. $|A_l|$ is the surface area of the corresponding face, and α corresponds to different Gaussian integration points $\mathbf{x}_\alpha$ and weights ω_α over the face. The weight and distribution of the quadrature points depend upon the order of the Gaussian quadrature rule employed, and for the present study suitable rules for the employed polynomial order are used. The interface fluxes are computed based on the boundary extrapolated reconstructed values, which are obtained by a polynomial reconstruction from element-averaged data.

The spatial discretisation is based on the approach of [8, 9] and lies in the the k-exact least square reconstruction, which is suitable for unstructured meshes with various types of element shapes in 2D and 3D, and it has been previously used successfully for laminar, transitional and turbulent flows [13, 46–53] and all the schemes are implemented in the UCNS3D CFD code as detailed in [52]. Therefore, only the key characteristics of this approach are going to be described in this paper. The main objective of the reconstruction process is to build a high-order polynomial $p_i(x, y, z)$ of arbitrary order r, for each considered element V_i that has the same average as a general quantity $\mathbf{U}_i$. This can be formulated as:

$$\mathbf{U}_i = \frac{1}{|V_i|} \int_{V_i} \mathbf{U}(x, y, z)\, dV = \frac{1}{|V_i|} \int_{V_i} p_i(x, y, z)\, dV. \tag{7}$$

The reconstruction process is performed in a transformed system of coordinates. The transformation is achieved by decomposing each element into tetrahedrals in 3D or triangles in 2D. This is done in order to minimize scaling effects that appear in stencils consisting of elements of different size as well as to improve the condition number of the system of equations [8, 13]. The reconstruction polynomial at the transformed cell V_i' is expanded over local polynomial basis functions labelled as $\phi_k(\xi, \eta, \zeta)$, which are given by:

$$p(\xi, \eta, \zeta) = \sum_{k=0}^{K} a_k \phi_k(\xi, \eta, \zeta) = \mathbf{U}_0 + \sum_{k=1}^{K} a_k \phi_k(\xi, \eta, \zeta), \tag{8}$$

where

$$\phi_k(\xi,\eta,\zeta) = \psi_k(\xi,\eta,\zeta) - \frac{1}{|V_i'|}\int_{V_i'} \psi_k(d\xi d\eta d\zeta), \qquad k = 1, 2, .., \tag{9}$$

with ψ_k being given by

$$\psi_k = \xi, \eta, \zeta, \xi^2, \eta^2, \zeta^2, \xi\eta, \xi\zeta, \eta\zeta..... \tag{10}$$

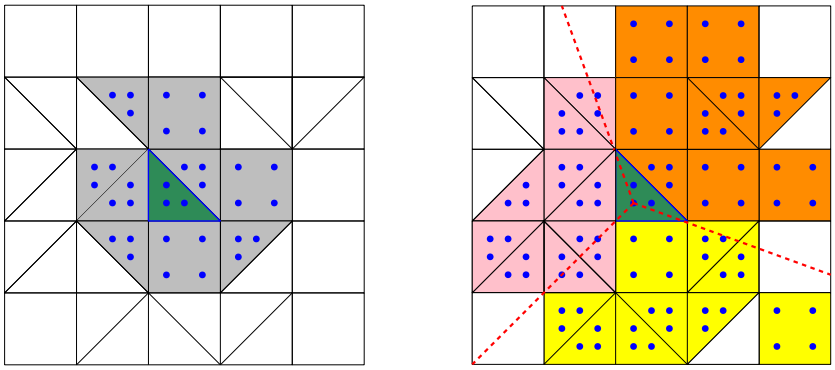

(a) Central stencil (b) WENO directional stencils

Figure 1: Schematic representation of stencils for a 3rd-order accurate scheme, with the considered cell filled with green colour and the blue dots representing the Gaussian quadrature points used for surface integrals in 2D, and the red dotted lines defining the geometrical sectors for the directional WENO stencils.

Additionally the unknown degrees of freedom a_k are constrained for each transformed cell in the stencil V_m',$m = 1, 2, .., M$ to have the same cell average of the reconstruction polynomial $p(\xi,\eta,\zeta)$ as the cell average of the solution $\mathbf{U}_m$:

$$\frac{1}{|V_m'|}\int_{V_m'} p(\xi,\eta,\zeta)(d\xi d\eta d\zeta) = \mathbf{U}_0 + \frac{1}{|V_m'|}\sum_{k=1}^{K}\int_{V_m'} a_k\phi_k(d\xi d\eta d\zeta) = \mathbf{U}_m, \tag{11}$$

where ξ, η, ζ are the coordinates in the reference system, and the upper index in the summation of expansion K is related to the order of the polynomial r by $K = \frac{1}{6}(r+1)(r+2)(r+3)-1$ for 3D and $K = \frac{1}{2}(r+1)(r+2)-1$ for 2D . For computing the degrees of freedom a_k, a minimum of K cells is required in the stencil in addition to the target cell. We utilise twice the number of required cells in the stencils as shown in Fig. 1, $M = 2K$, to improve the condition number of the linear system and improve the robustness of the method as described in [8, 54]. A linear least-square method is adopted to enable the system of equations of (8) for the unknown degrees of freedom a_k. The final form of the linear system is solved with the QR decomposition algorithm.

2.1.1. MUSCL

The MUSCL scheme employed in this work is based on the Barth and Jespersen slope limiter [55]. The design of this slope limiter requires the minimum and maximum values from the stencil formed by the considered cell i and the direct side neighbours:

$$\mathbf{U}_i^{min} = \min(\mathbf{U}_l : l = 1, ..., L) \quad and \quad \mathbf{U}_i^{max} = \max(\mathbf{U}_l : l = 1, ..., L), \tag{12}$$

where $l = 1, ..L$; L is the total number of direct-side neighbors of element i. The limiter seeks the minimum value of the slope limiter for all the faces l, and all the quadrature points α that satisfy the following conditions:

$$\phi_i = \min(\phi_{i,l,a}) \qquad l \in [1, N_f], \qquad \alpha \in [1, N_{qp}], \tag{13}$$

where $\phi_{i,l,\alpha}$ corresponds to the slope limiter value at a face and a quadrature point at the edges of the element i. Then, the limiting function is applied, composed by three different states according to the difference of the unlimited reconstructed value at the quadrature points of the considered element $\mathbf{U}_{(i,l,\alpha)}$, the minimum and maximum values from the neighbors $\mathbf{U}_l$, and the cell center value $\mathbf{U}_i$, yielding:

$$\phi_{i,\alpha} = \begin{cases} \min\left(1, \dfrac{\mathbf{U}_i^{max} - \mathbf{U}_i}{\mathbf{U}_{i,l,\alpha} - \mathbf{U}_i}\right), & \text{if } \mathbf{U}_{i,l,\alpha} - \mathbf{U}_i > 0 \\ \min\left(1, \dfrac{\mathbf{U}_i^{min} - \mathbf{U}_i}{\mathbf{U}_{i,l,\alpha} - \mathbf{U}_i}\right), & \text{if } \mathbf{U}_{i,l,\alpha} - \mathbf{U}_i < 0 \\ 1, & \text{if } \mathbf{U}_{i,l,\alpha} - \mathbf{U}_i = 0. \end{cases} \tag{14}$$

2.1.2. WENO

The WENO scheme employed in this study, utilises a non-linear combination of various reconstruction polynomials from the central stencil and the directional stencils as shown in Fig. 1 (b), where each polynomial is weighted according to the smoothness of its solution, and it is based on [8, 54]. The polynomials are given by:

$$p_i^{\text{weno}} = \sum_{m=1}^{m_s} \omega_m p_m(\xi, \eta, \zeta), \tag{15}$$

where m_s is the total number of WENO stencils. Substituting back to Eq. (8) for $p_m(\xi, \eta, \zeta)$, we obtain the following expression

$$p_m(\xi, \eta, \zeta) = \sum_{m=0}^{K} a_k^{(m)} \phi_k(\xi, \eta, \zeta). \tag{16}$$

Using the condition that the sum of all weights is unity, yields

$$\begin{aligned} p_i^{\text{weno}} &= \mathbf{U}_0 + \sum_{k=1}^{K} \left(\sum_{m=0}^{m_s} \omega_m a_k^m \right) \phi_k(\xi, \eta, \zeta) \\ &\equiv \mathbf{U}_0 + \sum_{k=1}^{K} \tilde{a}_k \phi_k(\xi, \eta, \zeta), \end{aligned} \tag{17}$$

where $\tilde{a}_k$ are the reconstructed degrees of freedom; and the non-linear weight ω_m is defined by [8, 13, 54]:

$$\omega_m = \frac{\tilde{\omega}_m}{\sum_{m=0}^{m_s} \tilde{\omega}_m} \quad \text{where} \quad \tilde{\omega}_m = \frac{\lambda_m}{(\epsilon + \mathcal{I}_m)^b}. \tag{18}$$

The smoothness indicator is given by:

$$\mathcal{I}_m = \sum_{1 \le |\beta| \le r} \int_{\tilde{E}_i} \left(\mathcal{D}^\beta p_m(\xi, \eta, \zeta) \right)^2 (d\xi, d\eta, d\zeta), \tag{19}$$

where β is a multi-index, r is the polynomial's order, λ_m is the linear weight and for this study the central stencil is assigned a large linear weight of $\lambda_1 = 1000$ and a value to prevent division by zero of $\epsilon = 10^{-6}$ is used similarly to [8, 9], and D is the derivative operator. The smoothness indicator is a quadratic function of the degrees of freedom (a_k^m) and can be expressed as a universal mesh-independent oscillation indicator matrix as defined by Dumbser et al. [54]. The WENO reconstruction is carried out in terms of conserved for the present study, in order to evaluate the impact of the (LM) treatment. The various reconstruction polynomials arise from different sets of stencils that satisfy certain geometrical conditions. The reader is referred to [8, 9] for the definition of geometrical sectors, and references therein, for a detailed explanation of the different set of geometrical conditions.

2.2. Low-Mach Number Treatment

For Godunov type schemes of first-order of accuracy, the theoretical analysis of Thornber et al. [31] demonstrated that there is an artificially large velocity jump at the cell interfaces at low Mach number regions, when using piecewise constant variable extrapolation. The solution proposed was instead of modifying the Riemann solver itself to compensate for the strengths of the acoustic waves, to modify the extrapolated reconstructed values at the cell interface in order to take into account the correct flow physics of low speed flows. It was also demonstrated for a 5th-order MUSCL scheme that the dissipation rate increases with the speed of sound and a simple solution to the problem was to modify normal and tangential velocity jumps at the cell interfaces by a function z as shown below:

$$\mathbf{u}_L^* = \frac{(1+z)\mathbf{u}_L + (1-z)\mathbf{u}_R}{2}, \qquad \mathbf{u}_R^* = \frac{(1+z)\mathbf{u}_R + (1-z)\mathbf{u}_L}{2}, \qquad z = min(1, max(M_L, M_R)). \tag{20}$$

where $\mathbf{u}_L^*$, $\mathbf{u}_R^*$ denotes the modified extrapolated vector of velocities for the left- and right-states respectively, and $\mathbf{u}_L$, $\mathbf{u}_R$ denotes the extrapolated vector of velocities for the left- and right-states respectively. The key advantage of this approach is its simplicity, and compactness since the extrapolated variables at the cell interfaces are only required, which are computed and stored from the solution of the Riemann problem. Additionally, the reconstructed extrapolated values for pressure and density are not modified since that would cause excessive diffusion in stationary contact surfaces [31].

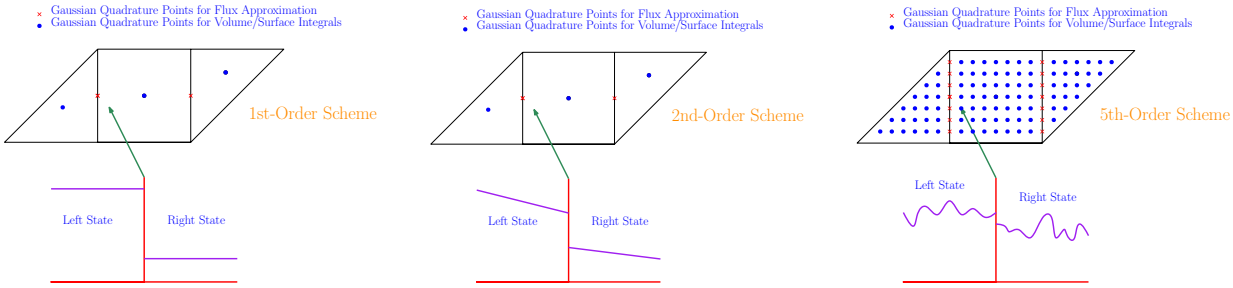

(a) 1st-order piecewise constant approximation

(b) 2nd-order piecewise linear approximation

(c) 5th-order scheme with quatric polynomial approximation

Figure 2: Schematic representation of intercell flux states for various schemes.

When considering the main difference of higher-order schemes to lower-order ones, apart from the piecewise constant, linear, quartic data representation as shown in Fig. 2, is that the velocity jumps between the left and right states are reduced for smooth flows. This is partially attributed to the fact that for high-order FV schemes, the size of the reconstruction stencil is proportional to the order of accuracy. This leads to a higher number of common elements in the stencils of two adjacent cells. For example, the percentage of common stencil elements between two adjacent cells increases from 40% for a 2nd-order scheme to 85% for a 5th-order scheme as shown in Fig. 3. Therefore the two states are more similar since their approximation is based on more similar spatial information.

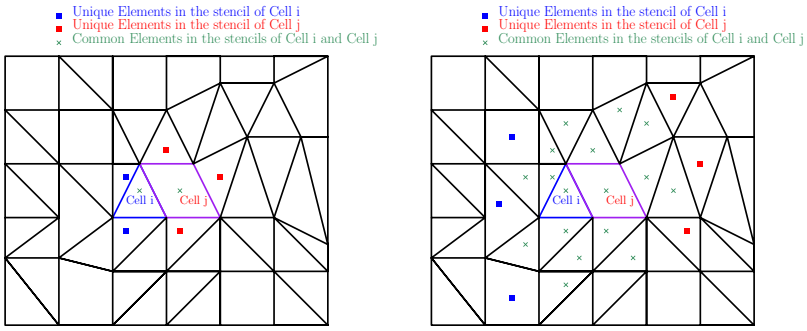

(a) 2nd-order (b) 3rd-order

Figure 3: Schematic of stencil neibourhood for 2^{nd}-order and 3^{rd}-order schemes for elements i and j, on a hybrid unstructured 2D domain.

Based on the findings of Rieper [45], demonstrating that the triangular meshes do not suffer from the accuracy problem for low Mach number flows as the quadrilateral meshes due to their increased degrees of freedom, and the observations of Thornber et al. [31] from the DIT test case that the tangential components of the velocity should need more numerical dissipation than the normal components, a similar LM treatment of Thornber et al. [31] is pursued. In this case only the normal components $\hat{n}$ of the velocity at the interfaces are modified, and not their tangential $n_{\|}$ as shown in Fig 4.

$$u_L^{\hat{n}*} = \frac{(1+z)u_L^{\hat{n}} + (1-z)u_R^{\hat{n}}}{2}, \qquad u_R^{\hat{n}*} = \frac{(1+z)u_R^{\hat{n}} + (1-z)u_L^{\hat{n}}}{2}, \qquad z = min(1, max(M_L, M_R)). \tag{21}$$

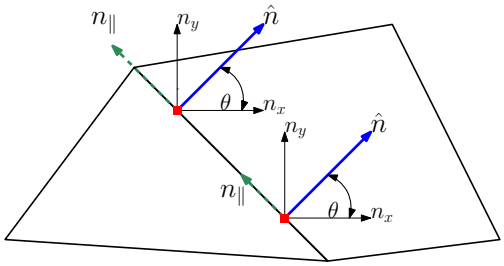

Figure 4: Schematic representation of normal vector components at the intercell edge between two elements, with the red coloured boxes representing the Gaussian quadrature points.

where $u_L^{\hat{n}*}$, $u_R^{\hat{n}*}$ denotes the modified extrapolated normal component of velocities for the left- and right-states respectively, and $u_L^{\hat{n}}$, $u_R^{\hat{n}}$ denote the reconstructed extrapolated values for the velocity in the direction normal to the face/edge for the left- and right-states respectively. This approach is also used by Oßwald et al. [39], with the Roe Riemann solver [43], labelled LMRoe, where higher dissipation is observed compared with the original implementation of Thornber et al. [31] for the DIT test case. The benefits offered of using the similar strategy as Oßwald et al. [39] LM treatment where only the normal components are modified in terms of accuracy, and robustness compared to the original implementation are explored. The local Mach number for the left and right states M_L, M_R are calculated based on the velocity magnitude of all the velocity components independent of the normal direction in which the flux is computed, similarly to Oßwald et al. [39].

2.3. Fluxes approximation & Temporal discretisation

For the evaluation of the convective fluxes the approximate HLLC (Harten-Lax-van Leer-Contact) Riemann solver of Toro [56] is used to compute the intercell numerical flux unless otherwise stated. For the evaluation of the viscous fluxes the extrapolated interface variables $U_{i,a}^{\pm}$ and their unlimited gradients $\nabla U_{i,a}^{\pm}$ from the k-exact least square reconstruction are averaged from two discontinuous states as detailed in [13, 57]. For the gradients additionally penalty terms are included following the formulation of Gassner et al. [58] for suppressing odd-even decoupling modes in the numerical solutions [59], in the following manner:

$$\nabla \mathbf{U} = \frac{1}{2}\left(\nabla \mathbf{U}_L + \nabla \mathbf{U}_R\right) + \frac{\alpha}{L_{int}}\left(\mathbf{U}_R - \mathbf{U}_L\right)\vec{n}, \tag{22}$$

where L_{int} is the distance between the cell centres of adjacent cells, and $\alpha = 4/3$ similarly to previous approaches [59, 60]. The solution is advanced in time by the explicit Strong Stability Preserving (SSP) Runge-Kutta 3^{rd}-order method [61], and a CFL of 0.9 is used for all the test-cases in the present study, unless otherwise stated.

3. Results

This section presents the results obtained for a variety of cases in two and three dimensions evaluating the use of the subject LM treatment. The five test cases presented examine the LM treatment's ability to resolve low-Mach number flow features while retaining the ability to solve the compressible equations without introducing numerical artefacts. The employed MUSCL and WENO schemes are frequently used for compressible flows that can include regions of smooth and sharp-gradients and their performance at the smooth regions of the flow is the primary focus of this study.

3.1. Subsonic flow past a 2D cylinder

The steady state inviscid flow past a circular cylinder with diameter $D = 1$ is considered. The cylindrical computational domain extends 15 diameters in all directions $D = 15$, with a free-stream Mach number of $M_\infty = 0.05$, and slip-wall boundary conditions imposed on the cylinder and pressure farfield boundary conditions imposed on the outer boundary. The flow is initialised with a flow direction parallel to the x-axis.

The simulations were initially undertaken on a hybrid mesh with $8,290$ elements. The mesh is shown in Fig. 5. The computations are undertaken for 10 convection times $t = 10t_c$, where $t_c = \frac{Diameter}{Velocity}$, which is sufficient for the initial transients to vanish and the solution to converge. The MUSCL and WENO schemes are employed, and the original low-Mach number treatment of Thornber et al. [31] denoted as LM1 given by Equation (20) and the proposed one as LM2 given by Equation (21).

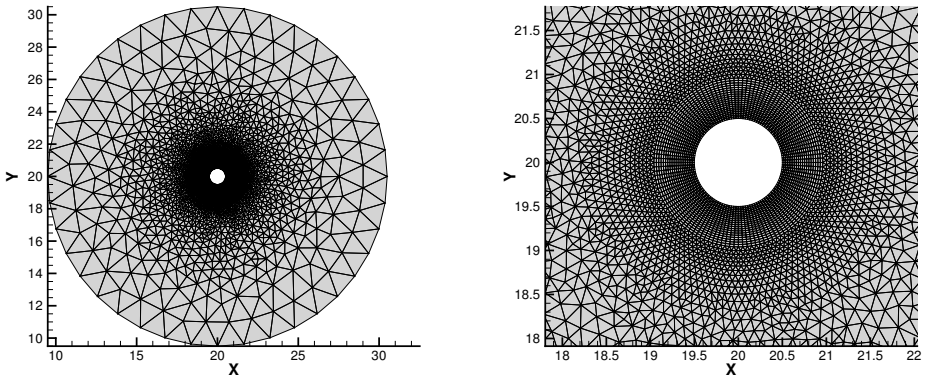

(a) Mesh overview

(b) Close-up of cylinder

Figure 5: Hybrid unstructured mesh used for the subsonic flow past a 2D cylinder.

The contour plots of Mach number at time $t = 10t_c$ obtained with MUSCL and WENO schemes can be seen in Fig. 6. Firstly, it is noticed that the original LM treatment of Thornber et al. [31] directly extended to hybrid unstructured grids fails to resolve the correct flow features, since artefacts appear in the solution that are independent of the type and order of the numerical scheme, and the grid resolution. This behaviour can be justified by the fact that triangles have different dissipation characteristics from quadrilateral elements, as analysed by Rieper [45]. Hybrid meshes include an interface between quadrilaterals and triangles and a similar simple, compact approach for LM treatment of the reconstructed values is desired. An algorithm that treats the quadrilaterals-triangle interfaces in a different manner from quadrilateral-quadrilateral interfaces would not have been of any value to higher-order FV schemes. The primary reason being that elements of different types are already included in the stencil and they affect the reconstructed solution.

When applying the low-Mach treatment to the normal vectors of the interfaces, a different behaviour is noticed. There is an improvement in terms of the correct flow pattern for the MUSCL 2^{nd}-order scheme as opposed to the results without any treatment. For WENO schemes the situation is slightly more complicated since an improvement is noticed only for the WENO 3^{rd}-order scheme. The combination of the WENO 5^{th}-order scheme at this resolution without any LM treatment is sufficient to provide the correct flow pattern. This supports the numerous previous studies [32, 41, 42] of improving the resolution at low Mach regions by achieving very high-order spatial accuracy, since the jumps between the two flux states are greatly minimised. However when the LM2 treatment is applied for the WENO 5^{th}-order scheme an incorrect solutions obtained. This complements previous studies where for higher-order WENO schemes these type of LM treatment can contaminate the solution even for structured grid arrangements [62].

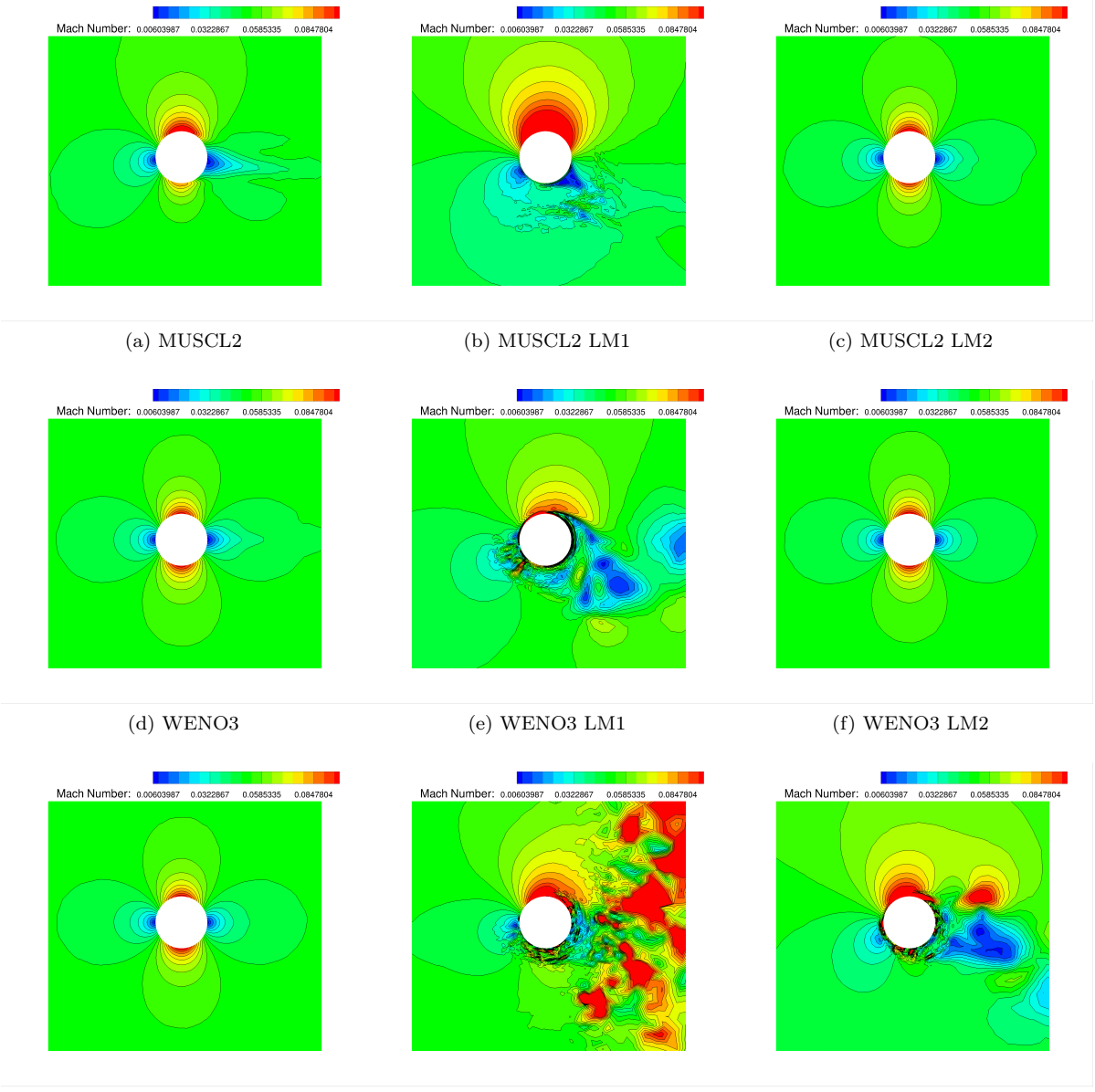

(a) MUSCL2 (b) MUSCL2 LM1 (c) MUSCL2 LM2

(d) WENO3 (e) WENO3 LM1 (f) WENO3 LM2

(g) WENO5 (h) WENO5 LM1 (i) WENO5 LM2

Figure 6: Contours of Mach number obtained from MUSCL and WENO numerical schemes for the subsonic flow past a 2D cylinder.

At the current grid resolution the LM2 treatment with the WENO 3^{rd}-order scheme, provide a better solution indicating that the jumps are sufficiently large for the treatment to provide some benefits.One question that arises following these results is how the WENO schemes will behave for this test problem if the grid resolution is substantially increased. For this purpose a finer hybrid mesh consisting of $139,910$ elements as seen in Fig.7 is employed with the WENO schemes and only the LM2 treatment, since we have not managed to obtain correct results with the LM1 treatment.

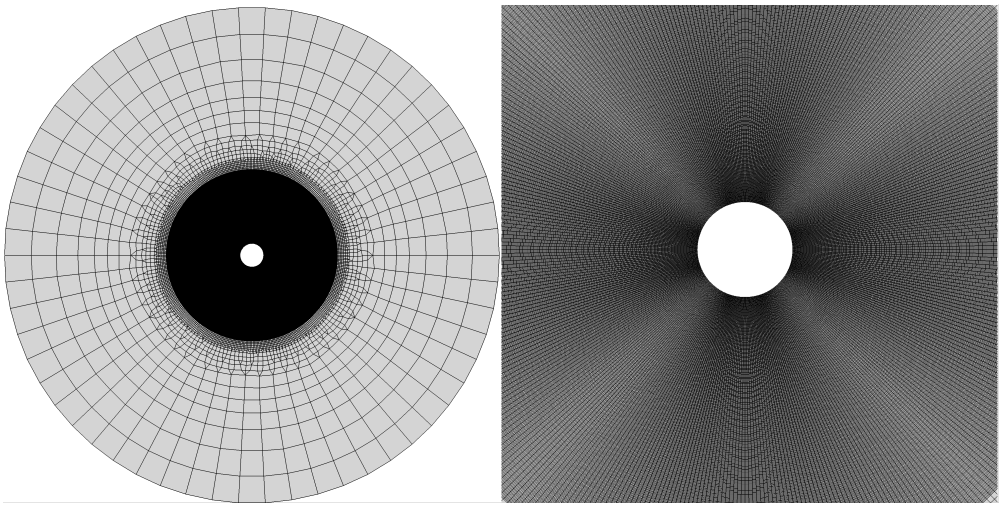

(a) Mesh overview (b) Close-up of cylinder

Figure 7: Finer hybrid unstructured mesh used for the subsonic flow past a 2D cylinder.

From the obtained results as seen in Fig.8 the same trend is observed. The WENO 3^{rd}-order scheme experiences some minor improvements in the results with the application of the LM2 treatment, the WENO 4^{th}-order scheme does not experience any significant differences in the results using the LM2 treatment, and on the other hand the WENO 5^{th}-order scheme results are incorrect when the LM2 treatment is employed, and correct when not employed. The primary reason for this behaviour is that as the order of accuracy is increased the jumps between the states is reduced, and the balance between dissipation and dispersion is altered. It needs to be stressed that this undesired behaviour can be controlled if a parametric investigation is pursued for the parameters contributing to the non-linear weights as seen in Eq. (18), namely the central stencil linear weight $\lambda_1 = 1000$ and the parameter used to prevent division by zero $\epsilon = 10^{-6}$. However this parametric investigation is beyond the scope of the present study.

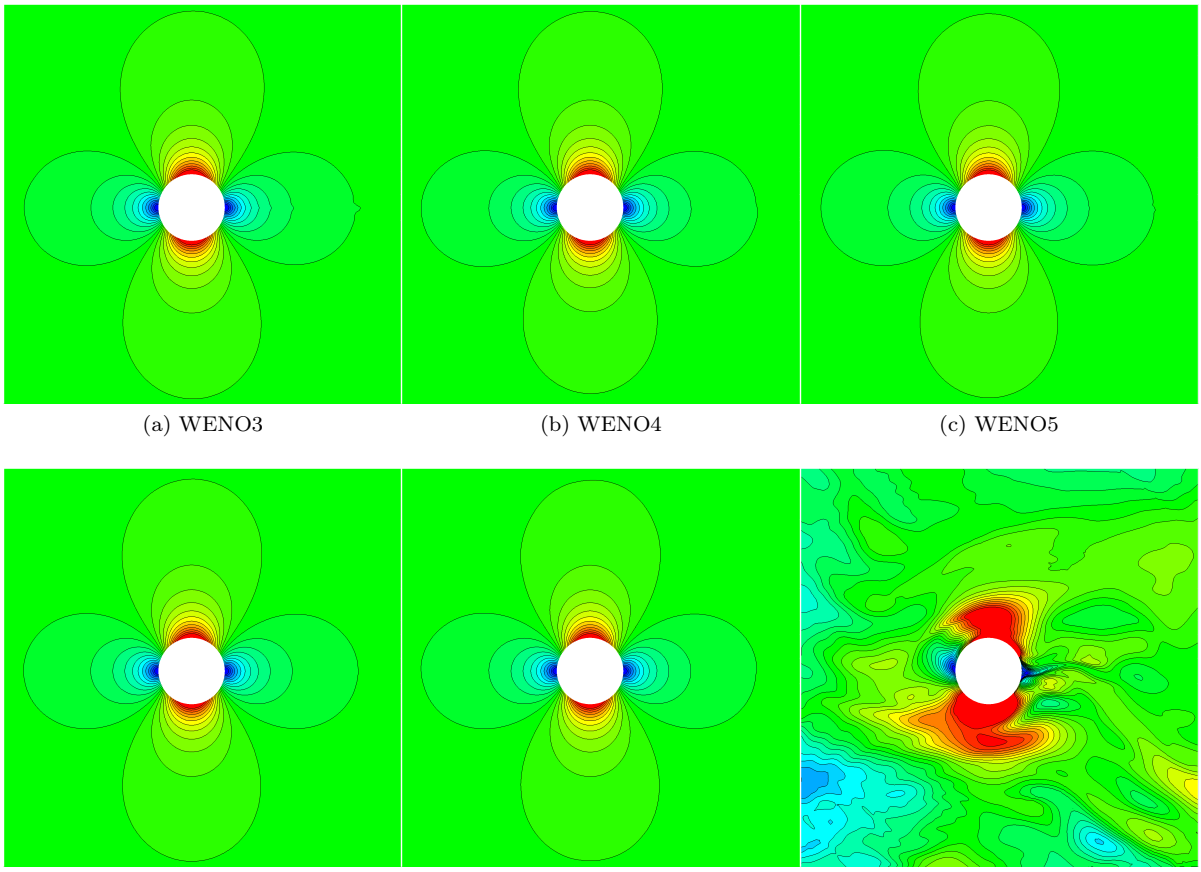

(a) WENO3 (b) WENO4 (c) WENO5

(d) WENO3 LM2 (e) WENO4 LM2 (f) WENO5 LM2

Figure 8: Contours of Mach number obtained from WENO numerical schemes for the subsonic flow past a 2D cylinder on the finest mesh, 24 contour levels equally spaced between $M = 0.01 - 0.09$.

Since for non-linear WENO schemes where the jumps between the states is significantly reduced compared to MUSCL 2nd-order schemes, any LM treatment should take into account apart from the velocity jumps, the dissipation, dispersion and monotonicity characteristics of the numerical scheme in conjunction with the grid-resolution. This behaviour suggest that the deployment of these type of treatments might provide some benefits for underesolved turbulent flow simulations. From this section onwards only the LM2 treatment will be considered (labelled as LM treatment onwards) since we were unable to obtain results free from artefacts with the original LM1 treatment of Thornber et al. [31] for all the test problems that follow.

3.2. Supersonic flow past a 2D cylinder

The unsteady inviscid supersonic flow past a circular cylinder of radius $r = 0.5$ is considered. The semi-cylindrical computational domain extends 2 diameters in all directions $D = 2$, with a free-stream Mach number of $M_\infty = 10.0$, a slip-wall boundary conditions imposed on the cylinder, supersonic outflow on the side outer boundaries, and supersonic inflow on the left semi-circular side of the domain.

The simulations were undertaken on a quadrilateral mesh consisting of $30,000$ elements (200×150) as seen in Fig. 9. The computations are undertaken for 10 convection times $t = 10t_c$, where $t_c = \frac{Diameter}{Velocity}$, which is sufficient for the initial transients to vanish, although the solution might not converge due to the unsteadiness behind the bow-shock. The MUSCL and WENO schemes are employed with and without the proposed low-Mach number treatment. For these particular flow regimes the region behind the strong

bow shock is subsonic, therefore it is of interest to evaluate the influence of the present low-Mach number treatment.

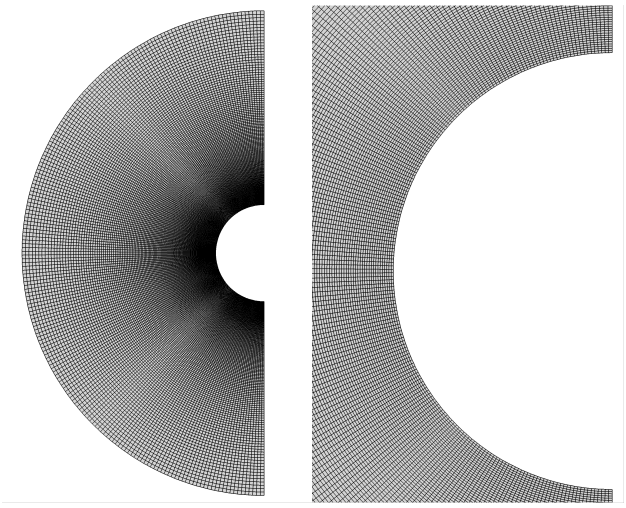

(a) Mesh overview (b) Close-up of cylinder

Figure 9: Quadrilateral mesh used for the supersonic flow past a 2D cylinder.

The HLLC Riemann solver for this flow problem is known to be prone to carbuncle and shock instabilities behind the bow shock [63] as also noticed for the present schemes in Fig. 10. Since it is not possible to determine the influence of the low-Mach number treatment using this Riemann solver, and although there are artificial viscosity techniques to alleviate this as documented by Rodionov [63] it is beyond the scope of the present study. Therefore the Rusanov [64] Riemann solver is employed which is known to be less prone to produce carbuncle and shock instabilities, so that the influence of the low-Mach number treatment can be evaluated.

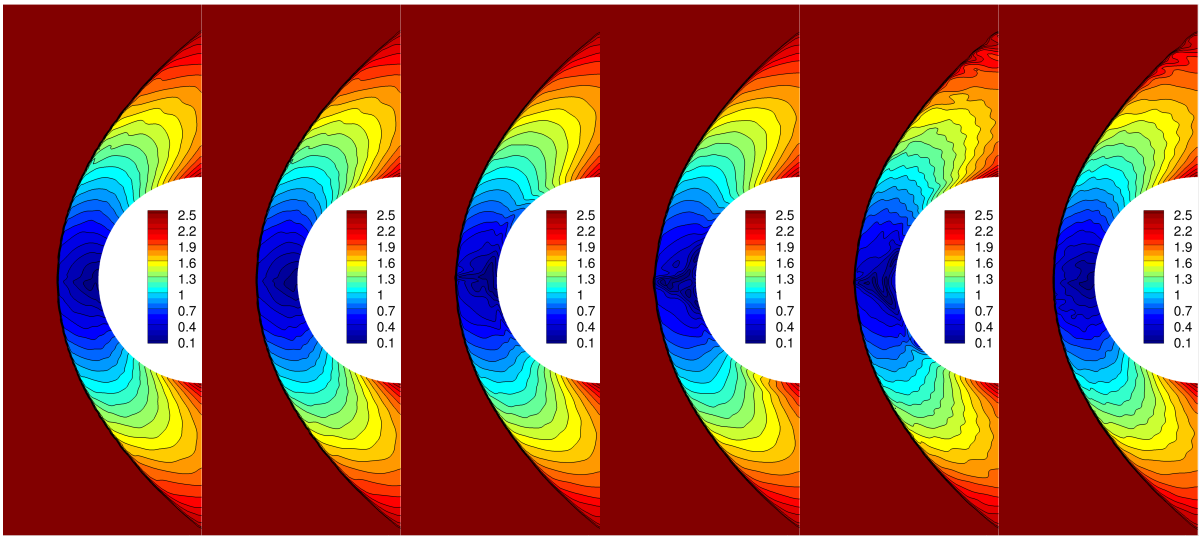

(a) MUSCL2 (b) MUSCL2 LM (c) WENO3 (d) WENO3 LM (e) WENO4 (f) WENO4 LM

Figure 10: Contours of Mach number obtained from various numerical schemes for the supersonic flow past a 2D cylinder test problem using the HLLC Riemann solver. Twenty five equally spaced Mach number contours from 0.1 to 2.5. All schemes prone to shock instabilities due to the HLLC Riemann solver employed.

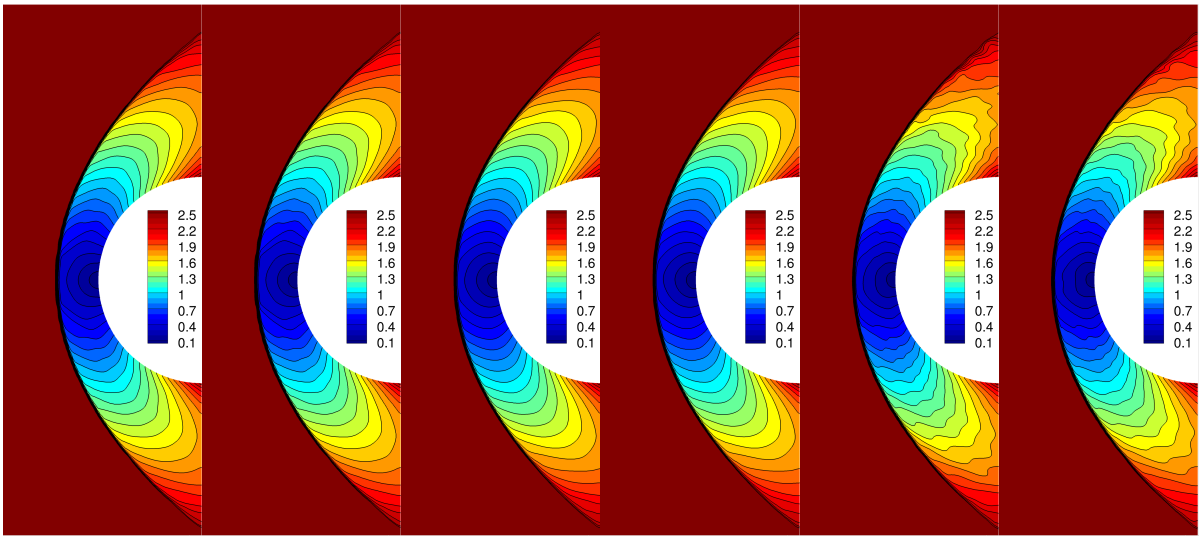

(a) MUSCL2 (b) MUSCL2 LM (c) WENO3 (d) WENO3 LM (e) WENO4 (f) WENO4 LM

Figure 11: Contours of Mach number obtained from various numerical schemes for the supersonic flow past a 2D cylinder test problem using the Rusanov Riemann solver. Twenty five equally spaced Mach number contours from 0.1 to 2.5.

The results obtained with the Rusanov Riemann solver do not exhibit any carbuncles and shock instabilities appearing as seen in Fig.11. When applying the low-Mach number treatment with MUSCL 2^{nd}-order and WENO 3^{rd}-order schemes there are not any significant differences in the results, which is the desired behaviour since the resolution at the low-Mach number region although quite close to the bow-shock is not deteriorated by the treatment. On the other hand when using the WENO 4^{th}-order scheme wiggles start appearing in the solution which are not related to the low-Mach number treatment. These wiggles are the

results of the reduced numerical dissipation of the scheme, and they initiate at the region behind the shock and propagate downstream. It needs to be stressed that the present treatment does not deteriorate the results in subsonic regions of supersonic flows, although a potential improvement could have been noticed if a boundary layer was resolved and the viscous Navier-Stokes equations solved since the Mach number very close to the wall would have been very small.

3.3. 2D vortex evolution

The second test-cases involves the flow of the two dimensional vortex evolution, as introduced in the 3^{rd} International Workshop on High-Order CFD Methods. The compressible Euler equations are solved in a 2D domain of $[0, 0.1]^2$ with periodic boundary conditions applied to all outer sides. The domain is initialised with a uniform pressure P_∞, temperature T_∞ and Mach number M_∞. A vortex is introduced of radius R and strength β, positioned at the centre of the domain (X_c, Y_c). The local u,v velocity components and temperature T are given by:

$$u = U_\infty \left(1 - \beta \cdot \frac{y - Y_c}{R} \cdot e^{-r^2/2}\right), \tag{23}$$

$$v = U_\infty \beta \cdot \frac{x - X_c}{R} \cdot e^{-r^2/2}, \tag{24}$$

$$T = T_\infty - \frac{U_\infty^2 \beta^2}{2C_p} \cdot e^{-r^2}, \tag{25}$$

where the heat capacity at constant pressure C_p is given by:

$$C_p = R_{gas} \frac{\gamma}{\gamma - 1}, \tag{26}$$

and the nondimensionalised distance r to the vortex core position is:

$$r = \frac{\sqrt{(x - X_c)^2 + (y - Y_c)^2}}{R}. \tag{27}$$

The free stream velocity U_∞ is given by the definition of:

$$U_\infty = M_\infty \sqrt{\gamma R_{gas} T_\infty}, \tag{28}$$

and the fluid pressure p, temperature T and density ρ are prescribed as follows:

$$\rho_\infty = \frac{p_\infty}{R_{gas} T_\infty}, \qquad \rho = \rho_\infty \left(\frac{T}{T_\infty}\right)^{\frac{1}{\gamma - 1}}, \qquad p = \rho R_{gas} T, \tag{29}$$

with $P_\infty = 10^5 N/m^2$, $T_\infty = 300K$. The "slow" vortex is considered with $\beta = 1/50$, and $R = 0.005$, that corresponds to a Mach number of $M_\infty = 0.05$. Ideally, the vortex should be transported without distortions by the flow and the initial condition is the reference solution to be compared with the computed solution and determine its accuracy.

The aim of employing this problem is to evaluate the capabilities of the LM treatment to preserve vorticity in an unsteady inviscid flow by employing the WENO reconstruction with spatial orders of accuracy ranging from 2^{nd}-order to 7^{th}. Meshes consisting of purely quadrilateral and triangular elements are considered, of various resolutions. In addition, randomly perturbed meshes based on the uniform quadrilateral and triangular elements are considered, that are randomly perturbed by a maximum distance of $\delta_{max} = 0.15D$ in both x,y Cartesian coordinates with D being the diameter of inscribed circle of the elements. The meshes are shown in Fig. 12 and the mesh statistics are outlined in Table 1.

The simulation is run for $T = 50t_c$ convective periods, with a period being given by $t_c = Length/U_\infty$, since maintaining the correct vortex pattern over a long period of time is the primary focus of this test

problem.

Table 1: Mesh statistics for the 2D vortex evolution test problem.

Mesh Name	Edges per side	Quadrilaterals	Triangles
UPQ32,PQ32	32	1024	-
UPQ64,PQ64	64	4096	-
UPQ128,PQ128	128	16384	-
UPT32,PT32	32	-	2048
UPT64,PT64	64	-	8192
UPT128,PT128	128	-	32768

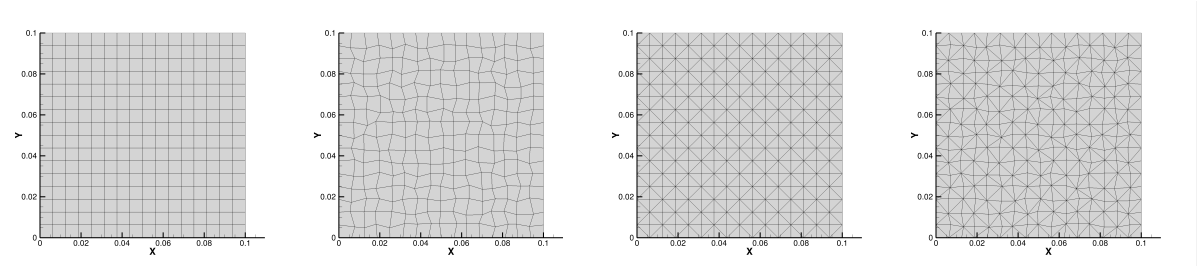

(a) Quadrilateral mesh (b) Quadrilateral perturbed mesh (c) Triangular mesh (d) Triangular perturbed mesh

Figure 12: Coarse meshes used for the vortex evolution test in two space dimensions.

All grid resolutions used apart from the finest (128 edges) meshes, are considered to be relatively coarse for the vortex evolution of this particular test case. This scenario is representative of the resolutions used close to the boundary layer of LES simulations, since for these low Mach number flow regions it is expected to correspond to a severely underesolved simulation. It is evident from Fig. 13 that the vortex distortion is increased as the number of periods increase, even for a WENO 3^{rd}-order scheme on the UPT64 mesh, suggesting that very high-order schemes might be required to maintain the vortex structure after 50 periods.

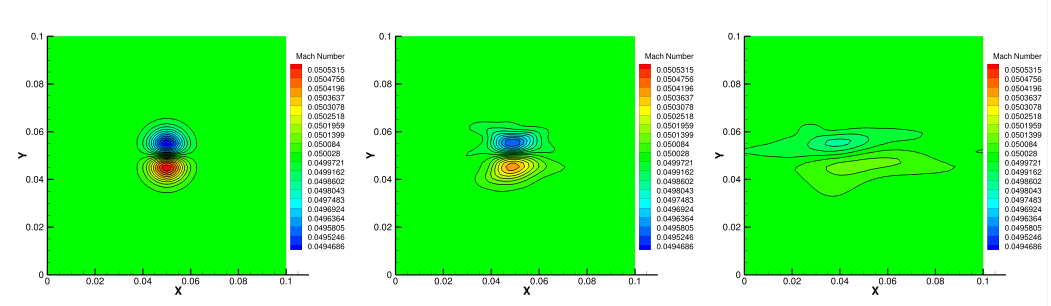

(a) $t = 0$ (b) $t = 5t_c$ (c) $t = 50t_c$

Figure 13: Mach number contour plots at different times for the vortex evolution test in two space dimensions obtained with a WENO 3^{rd}-order scheme on the UPT64 triangular mesh without low-Mach number treatment.

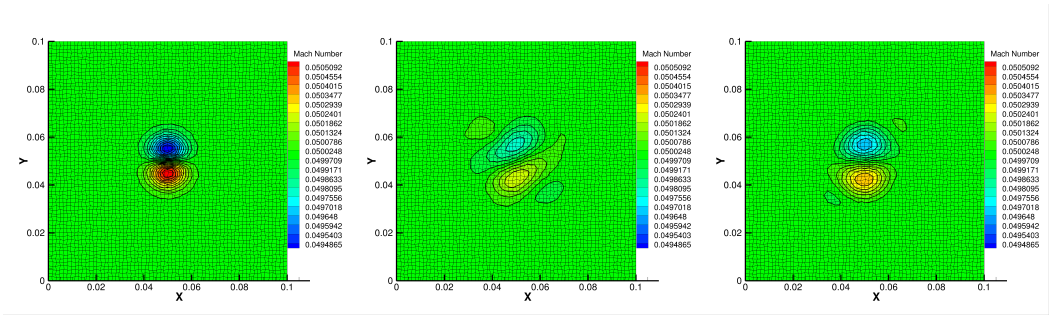

(a) $t = 0$ (b) $t = 50t_c$ (c) $t = 50t_c$ LM

Figure 14: Mach number contour plots on top of mesh overlay for the vortex evolution test in two space dimensions obtained with a WENO 7^{th}-order scheme on the PQ64 perturbed quadrilateral mesh

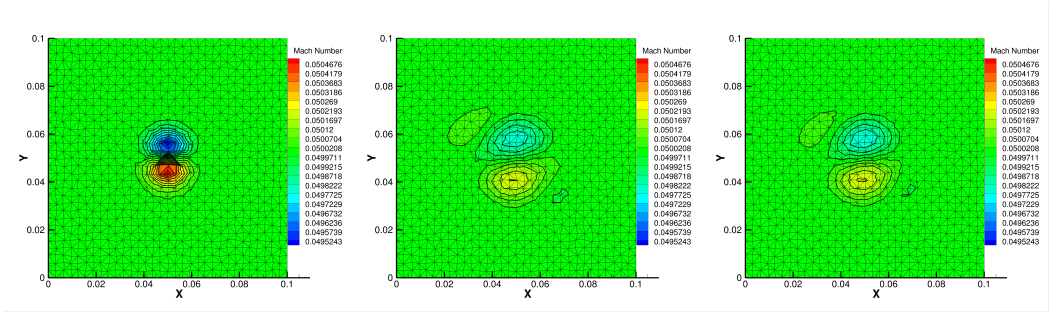

(a) $t = 0$ (b) $t = 50t_c$ (c) $t = 50t_c$ LM

Figure 15: Mach number contour plots for the vortex evolution test in two space dimensions obtained with a WENO 7th-order scheme on the PT32 perturbed triangular mesh.

The 7^{th}-order scheme with LM treatment, demonstrates decreased distortions in the vortex structure compared with the solution of the same schemes on the PQ64 mesh without LM fix, as shown in Fig. 14 where the bounds of the contour plots remain closer to their reference values. This trends is not present for the solution on triangular mesh where there are not as significant benefits as for the quadrilateral cells with the employment of the LM treatment as demonstrated in Fig. 15.

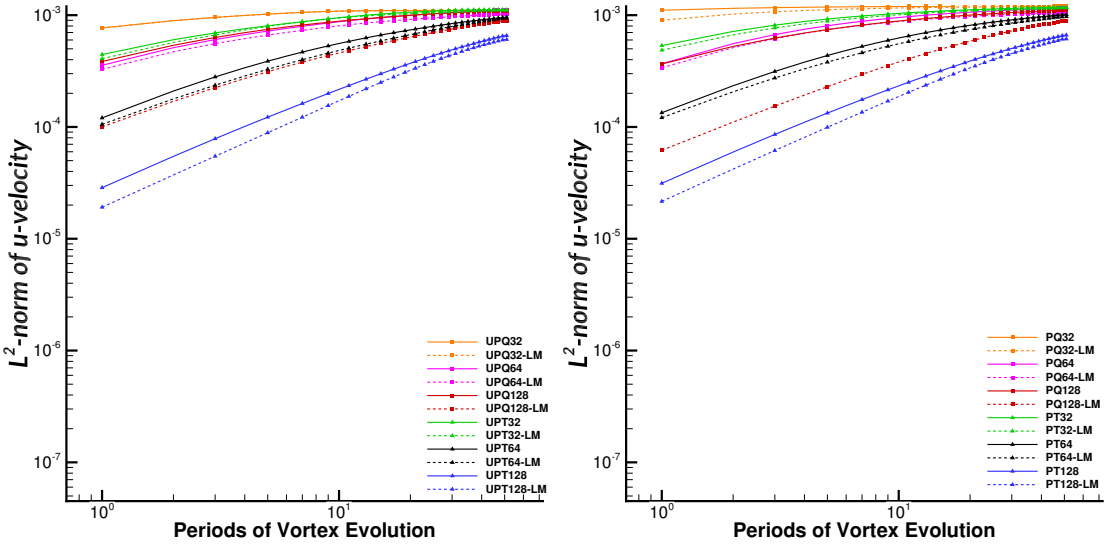

(a) Unperturbed Elements (b) Perturbed Elements

Figure 16: Evolution of $\mathcal{L}_2$ error of u velocity over 50 periods for the WENO 3^{rd}-order schemes on unperturbed and perturbed meshes for the vortex evolution test in two space dimensions.

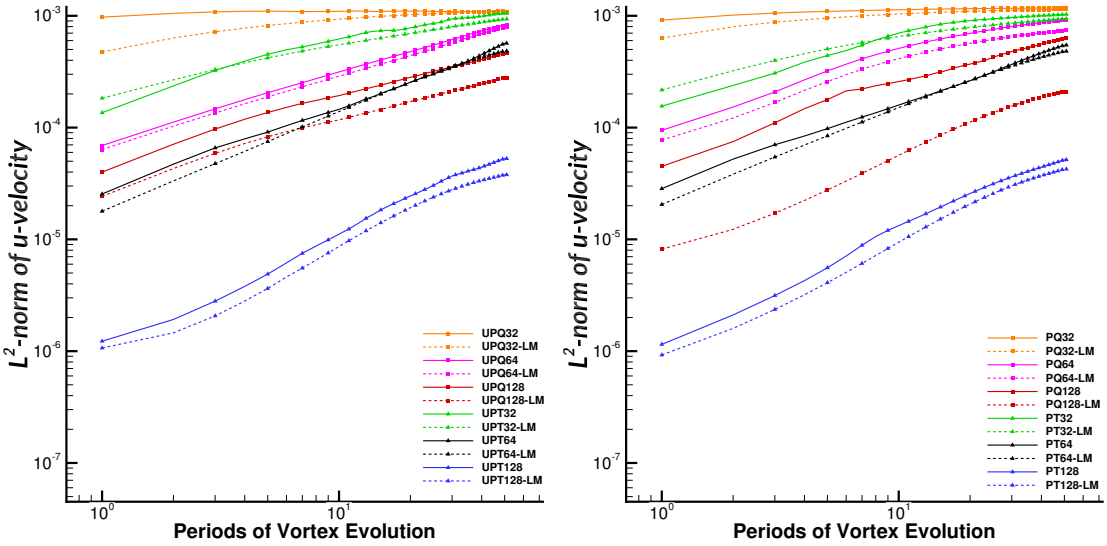

(a) Unperturbed Elements (b) Perturbed Elements

Figure 17: Evolution of $\mathcal{L}_2$ error norm of u velocity over 50 periods for the WENO 5^{th}-order schemes on unperturbed and perturbed meshes for the vortex evolution test in two space dimensions.

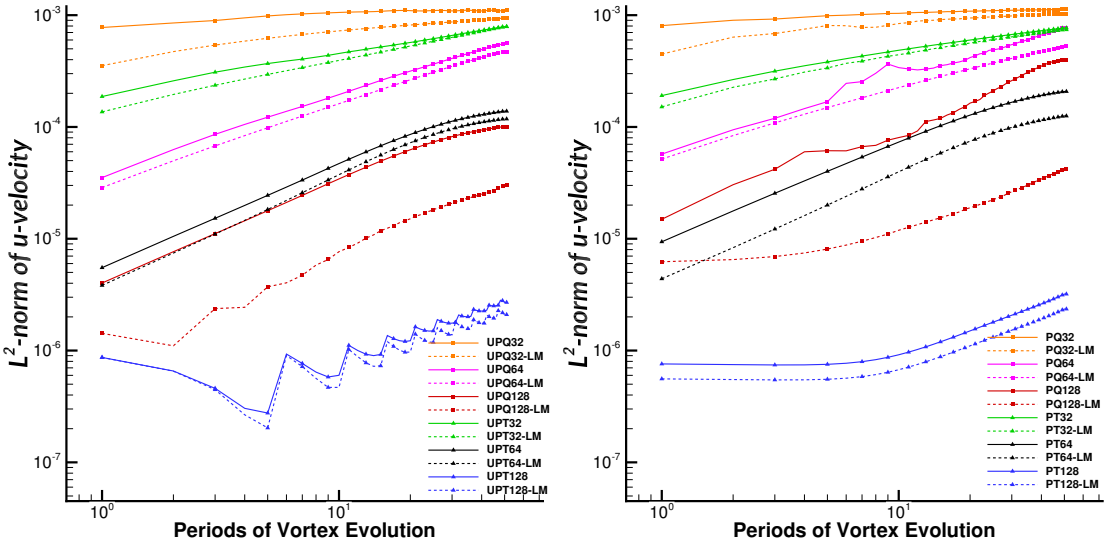

(a) Unperturbed Elements (b) Perturbed Elements

Figure 18: Evolution of $\mathcal{L}_2$ error norm of u velocity over 50 periods for the WENO 7^{th}-order schemes on unperturbed and perturbed meshes for the vortex evolution test in two space dimensions.

The evolution of the $\mathcal{L}_2$ error norm for 3^{rd}-, 5^{th}- and 7^{th}-order schemes on all mesh types, and resolutions are shown in Fig. 16, Fig. 17, and Fig. 18 respectively. It is noticed, that for the grid resolutions of 32 edges per side, the 5^{th}- and 7^{th}-order schemes benefit the most from the LM treatment, since this grid resolution is quite coarse. For all the schemes we notice a smaller error for the entire duration of the vortex evolution when the LM treatment is utilised. The impact of this treatment is more pronounced on grid resolutions comprised of 32 edges per side of the quadrilateral meshes (PQ32, UPQ32), and mostly with WENO 7^{th}-order scheme. Even the triangular meshes for all the numerical schemes and all the grid resolutions benefit from the low-Mach treatment but not as much as the quadrilateral cells.

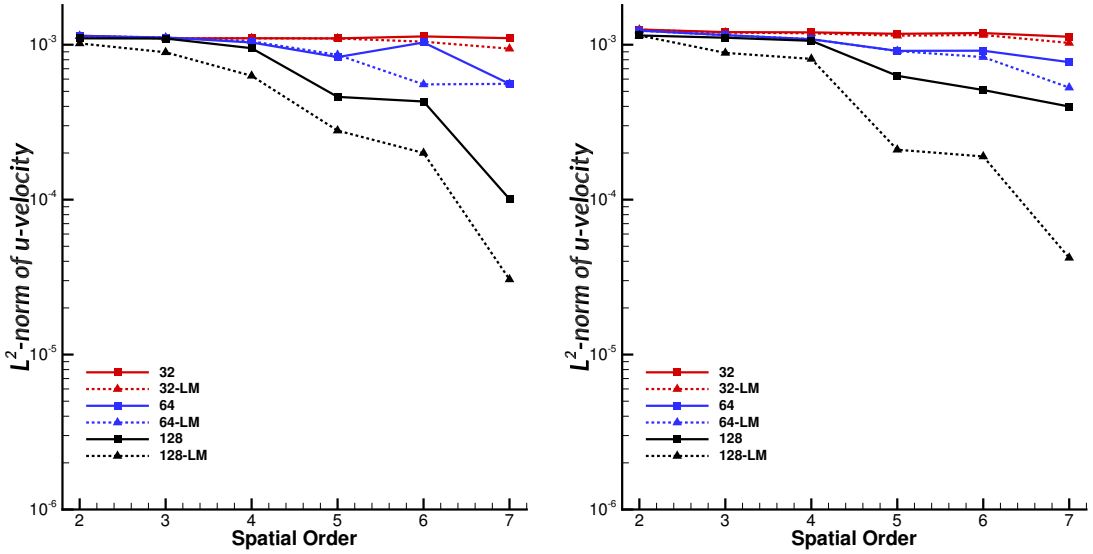

(a) Unperturbed Quadrilateral Meshes

(b) Perturbed Quadrilateral Meshes

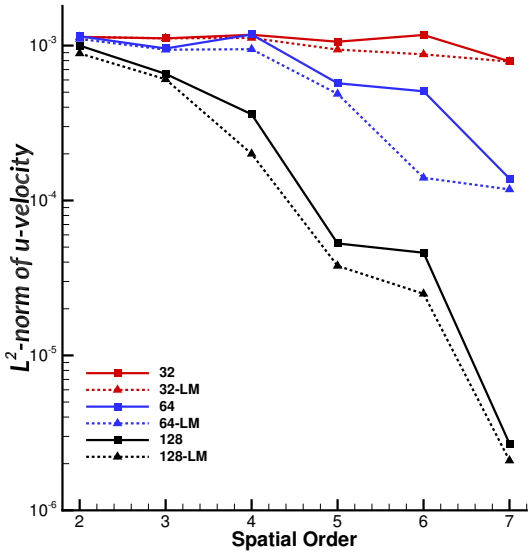

(c) Unperturbed Triangular Meshes

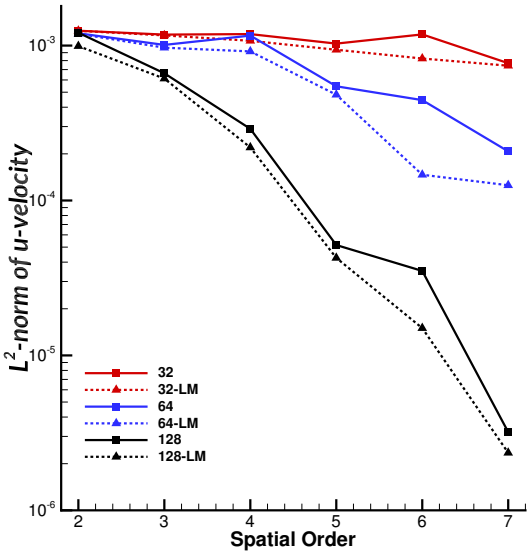

(d) Perturbed Triangular Meshes

Figure 19: $\mathcal{L}_2$ error norm of u velocity at 50 periods for all the schemes on unperturbed and perturbed meshes for the vortex evolution test in two space dimensions.

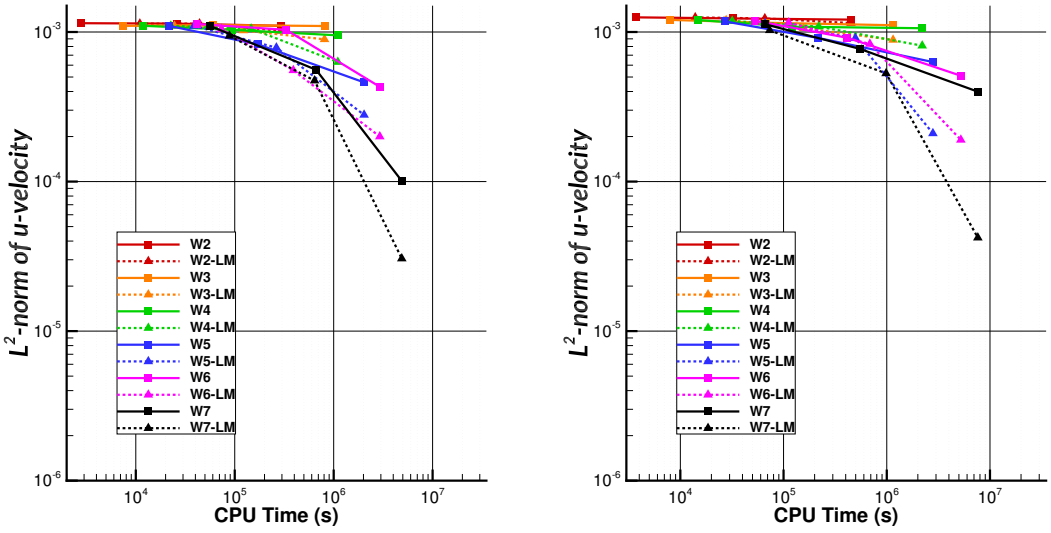

(a) Unperturbed Quadrilateral Meshes

(b) Perturbed Quadrilateral Meshes

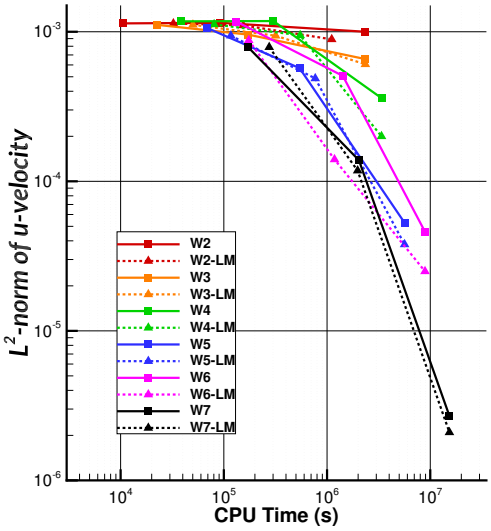

(c) Unperturbed Triangular Meshes

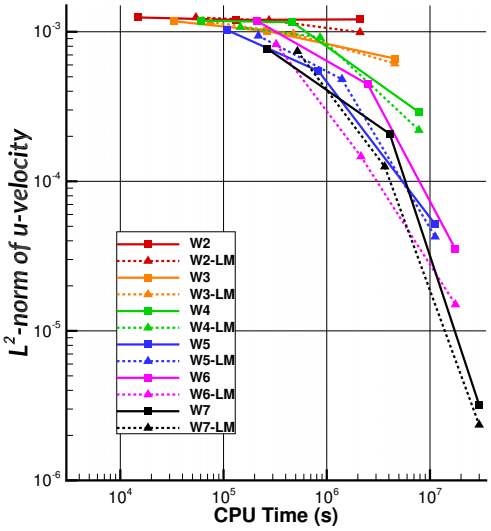

(d) Perturbed Triangular Meshes

Figure 20: $\mathcal{L}_2$ error norm of u velocity at 50 periods with respect to CPU time (Number of CPUs x Wallclock Time in seconds) for all the schemes on unperturbed and perturbed meshes for the vortex evolution test in two space dimensions.

The variations of $\mathcal{L}_2$ error norm after 50 periods with respect to the spatial order of accuracy for all the mesh types and resolutions are shown in Fig. 19. The predictions do not considerably differ between the perturbed and unperturbed meshes, since the employed WENO schemes remove scaling effects by transformation to a reference system as detailed in [8]. The computed solutions indicate that with the LM treatment there is an improvement in the predictions of all mesh types and schemes. However, the solutions obtained with the LM treatment have a consistent variation as the spatial-order of accuracy is increased. Specifically, the greatest improvement is observed for the 4^{th}-order and 6^{th}-order scheme corresponding to a 3^{rd}- and 5^{th}-order polynomial, respectively. This behaviour suggest that it could be related to the odd-order polynomials and their associated dispersion characteristics, which is amplified by the relatively coarse grid

resolutions employed for this study. Moreover, the step pattern observed with the 7^{th}-order scheme on the unperturbed meshes could be associated with the time-step selection and the CFL number utilised, since it is not evident on the corresponding perturbed meshes where their time-step is smaller due to the distortion of the mesh and the smaller radius of inscribed circle within each element. Since our temporal scheme is 3^{rd}-order accurate, it could suggest that the combination of a 7^{th}-order accurate scheme in space requires a smaller time step than the one defined by the CFL condition, due to the limited computational budget available a sensitivity to the time-step size could be pursue in the future.

The variation of $\mathcal{L}_2$ error norm after 50 periods with respect to the CPU time for all the mesh types, and numerical schemes is shown in Fig. 20. The LM treatment provides some benefits in terms of computational efficiency. A solution can be obtained with a lower-order scheme with the LM treatment at smaller computational budget compared with a higher-order schemes without LM fix with similar accuracy. For example, a 6^{th}-order scheme with the LM treatment requires significantly less time to reach the same level of error as a 7^{th}-order scheme without any treatment.

Therefore, the fact that the original implementation of the LM treatment by Thornber et al. [31] has been primarily focused on improving the behaviour of the schemes for underesolved simulated flows, comes into play in this test-case since the combination of all the schemes and all grid types benefit from the LM treatment both in terms of vortex structure resolution and computational efficiency.

3.4. 3D Taylor-Green vortex

The inviscid Taylor-Green vortex flow is considered as the first three dimensional cases for this work. The flow is benchmark cases for evaluating the vortex stretching and dissipation characteristics of numerical schemes by studying the production and break-down of turbulence structures. It has been widely employed by many authors to assess the behaviour of various numerical schemes [13, 65–70], in the context of Implicit Large Eddy Simulation (ILES) and how the numerical schemes themselves can possess characteristics that can potentially act as a Sub-Grid Scale (SGS) model. The DNS results of Brachet et. al [71] are used for reference. The computational domain is defined as $\Omega = [0, 2\pi]^3$ with periodic boundary conditions. This formulation of the Taylor-Green vortex flow problem is initialized with the following velocity and pressure fields:

$$u(x, y, z, 0) = sin(kx)cos(ky)cos(kz), \tag{30}$$

$$v(x, y, z, 0) = -cos(kx)sin(ky)cos(kz), \tag{31}$$

$$w(x, y, z, 0) = 0, \tag{32}$$

$$\rho(x, y, z, 0) = 1, \tag{33}$$

$$p(x, y, z, 0) = 100 + \frac{\rho}{16}[cos(2z) + 2] \cdot [cos(2x) + cos(2y)]. \tag{34}$$

The subject initial condition corresponds to an initial Mach number $M \approx 0.08$, with $k = 2\pi/\lambda = 1$ being the wavenumber. Simulations were carried out using the MUSCL 2^{nd}-order, WENO-3^{rd}, and WENO-5^{th} order schemes with two different types of meshes consisting of hexahedral and tetrahedral elements as shown in Fig. 21 and with the mesh statistics outlined in Table 2. Higher-order schemes of 6^{th}- and 7^{th}-order of accuracy were not pursued due to the computational budget available. All the simulations were intentionally performed in coarse meshes, to determine the impact of the LM treatment with the subject numerical schemes employed in obtaining physically meaningful results for underesolved simulation. The simulations were run up to $t = 20$ for obtaining the dissipation statistics. The evolution of large symmetrical structures to smaller ones transit to fully turbulent flow is illustrated in Fig. 22.

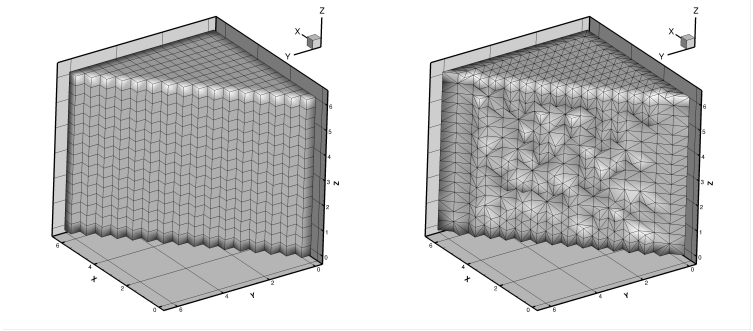

(a) Hexahedral mesh (b) Tetrahedral mesh

Figure 21: Coarse meshes used for the 3D Taylor-Green vortex test problem.

Table 2: Mesh statistics for the 3D Taylor-Green vortex test problem.

Mesh Name	Edges per side	Hexahedrals	Tetrahedrals
16H	16	4096	-
32H	32	32768	-
64H	64	262144	-
16T	16	-	24576
32T	32	-	196608
64T	64	-	1572864

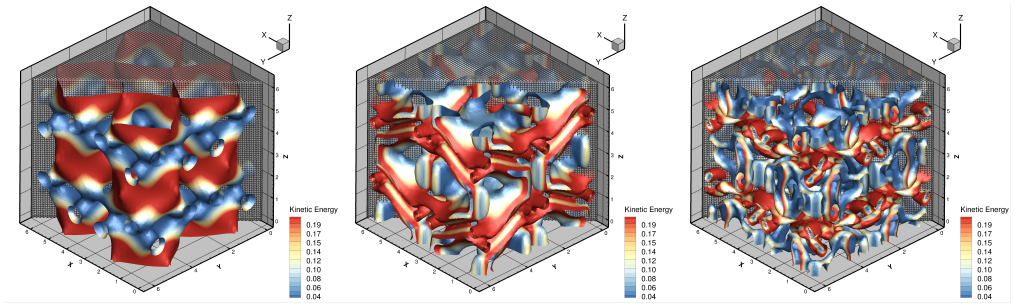

(a) $t = 1.07$ (b) $t = 4.47$ (c) $t = 6.63$

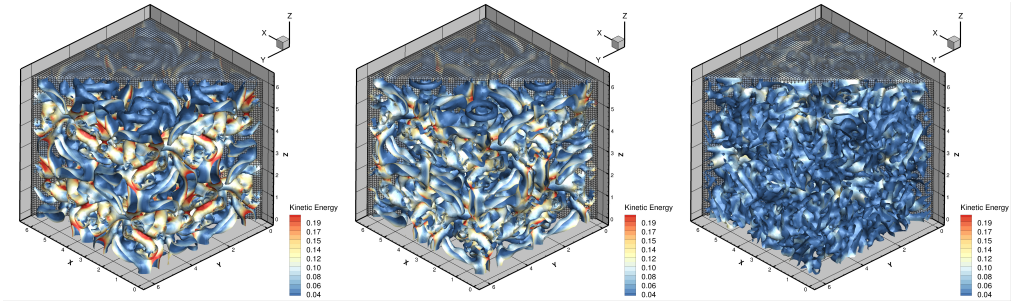

(d) $t = 9.90$ (e) $t = 10.99$ (f) $t = 16.61$

Figure 22: Isosurfaces of Q criterion at $Q = 0.5$, coloured by kinetic energy at different instants for the 3D Taylor-Green vortex test problem using a WENO 5^{th}-order scheme on the finest 64H hexahedral mesh with the LM treatment.

Since our aim is to employ the present numerical schemes without resorting to an explicit SGS model, the behaviour of the dissipation mechanism with respect to the LM treatment is of interest. Plotted in Fig. 23, Fig. 24, and Fig. 25 is the volumetrically averaged kinetic energy decay in time for both hexahedral and tetrahedral elements in three different resolutions: 16^3, 32^3 and 64^3. The results of Shu [70], using a structured WENO-5^{th} order accurate scheme are also included for comparison. The volumetrically averaged kinetic energy decay is typically applied as a mean of quantifying the numerical dissipation of a scheme. From the plots in Fig. 23, Fig. 24, and Fig. 25 it can be observed that the tetrahedral meshes outperform the hexahedral meshes in terms of dissipation characteristics when the LM treatment is not used which agrees with the findings of a previous study by Tsoutsanis et al. [13], due to their stencils more compact design when comparing the same order of accuracy. For the tetrahedral meshes there are not a significant benefits with the LM treatment; however, the treatment greatly improves the dissipation characteristics for hexahedral elements and especially for the MUSCL 2^{nd}-order scheme. It can be seen that at the coarsest resolution of the present hexahedral meshes the obtained results are closer to that of Shu [70]. At the medium grid resolution, all orders of accuracy can obtain a solution with similar dissipative characteristics of the Shu [70] results of the 5^{th}-order on a finer grid (64^3 vs. 32^3). The results obtained with the finest hexahedral meshes exhibit an improvement over the Shu [70] small mesh while the 64^3 LM treatment with WENO-5^{th} order scheme matches that of the Shu [70] on the 128^3 mesh.

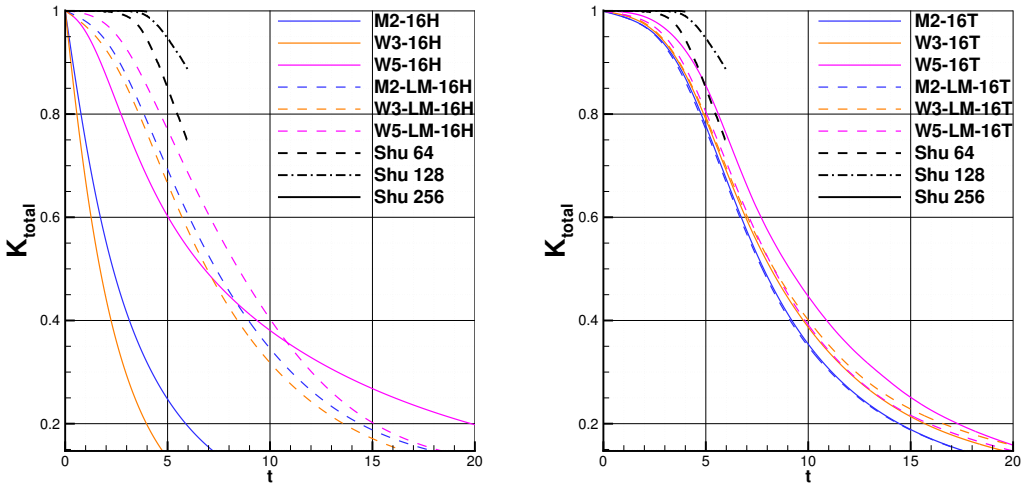

(a) Hexahedral (b) Tetrahedral

Figure 23: Total kinetic energy K temporal evolution for various schemes, and LM treatment for the 3D Taylor-Green vortex test problem at the coarse grid resolutions, and comparison with the WENO obtained solutions of [70].

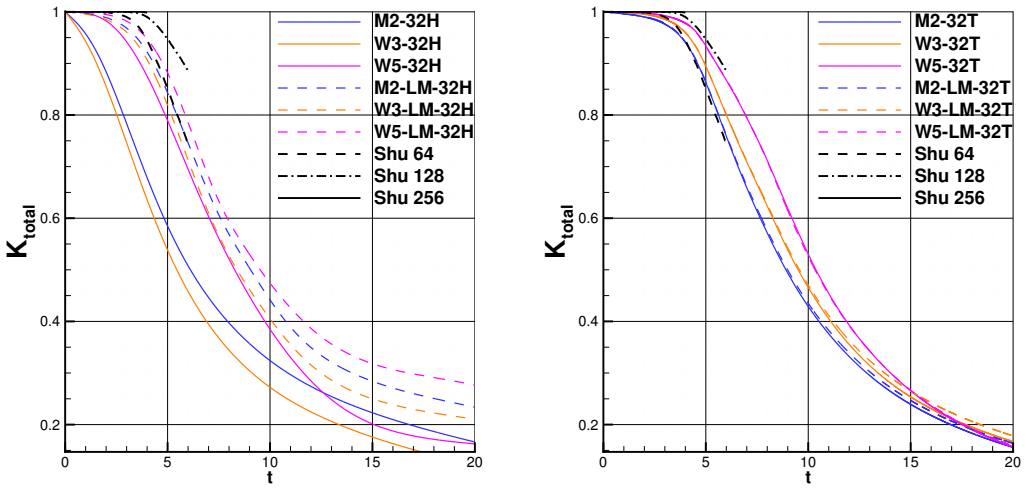

(a) Hexahedral (b) Tetrahedral

Figure 24: Total kinetic energy K temporal evolution for various schemes, and LM treatment for the 3D Taylor-Green vortex test problem at the medium grid resolutions, and comparison with the WENO obtained solutions of [70].

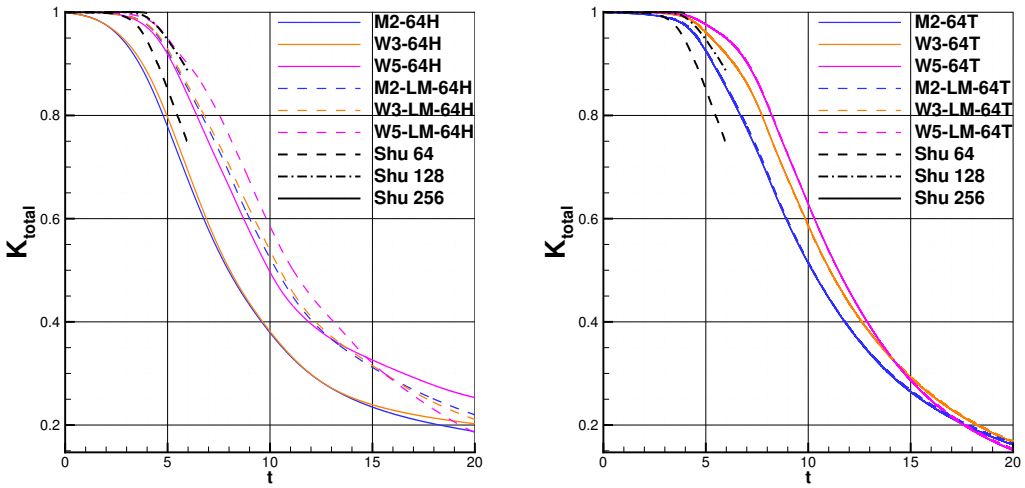

(a) Hexahedral (b) Tetrahedral

Figure 25: Total kinetic energy K temporal evolution for various schemes, and LM treatment for the 3D Taylor-Green vortex test problem at the finest grid resolutions, and comparison with the WENO obtained solutions of [70].

By computing the kinetic energy dissipation rate $-dK/dt$ as shown in Fig. 26, Fig 27, and Fig 28, it is possible to examine the resolved physical viscosity (or corresponding Reynolds number) and the inherent numerical dissipation. It can be seen that as the mesh resolution increases or if the order of accuracy increases the kinetic energy dissipation rates approach the DNS results of Brachet et al. [71] at higher Reynolds number. The tetrahedral meshes tend to a higher Reynolds number than their equivalent hexahedral meshes without the LM treatment. Considerable improvements are noticed for the hexahedral type simulations with respect to kinetic energy dissipation rate estimations with the LM fix. The additional structure predicted near $t \approx 5-6$ for the finest grid resolution are attributed to specific aspects of the ILES framework provided by the numerical schemes, and are present mostly in multidimensional numerical schemes as outlined in [65]. Furthermore, the double-peak structure of the dissipation rate near $t \approx 9$ for the finest tetrahedral

meshes with WENO schemes, has been previously [65] linked to dispersive properties of the scheme, since dissipative schemes do not exhibit this structure. This in turn highlights that the tetrahedral meshes are mostly susceptible to dispersion errors rather than dissipative errors, as seen by the noise in their the kinetic energy dissipation rate $-dK/dt$ in Fig. 26, Fig 27, and Fig 28 for WENO 5^{th}-order scheme, that is more prominent in the coarse grid resolution. Further investigation of this mechanism is to be pursued in the near future.

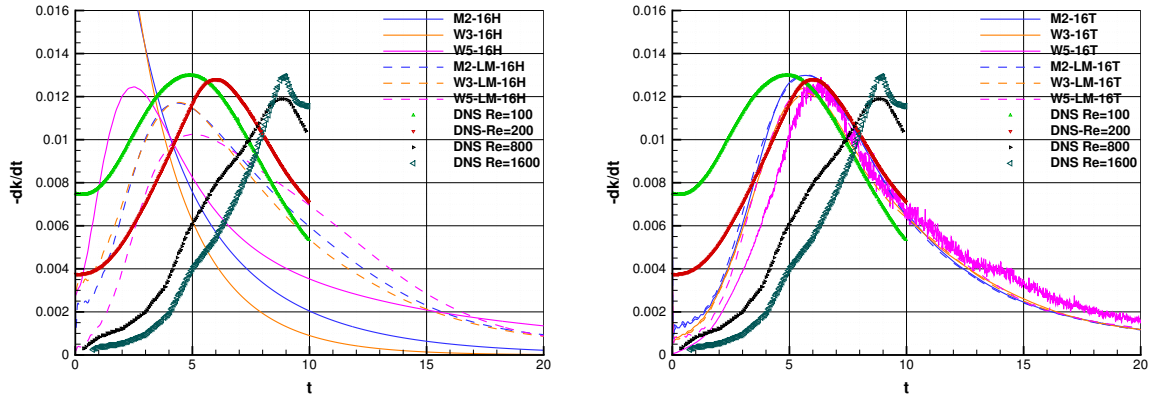

(a) Hexahedral 16H (b) Tetrahedral 16T

Figure 26: Total kinetic energy dissipation rate dK/dt temporal evolution for various schemes, grid resolutions, and LM treatment for the 3D Taylor-Green vortex test problem, and comparison with the DNS reference solutions of [71].

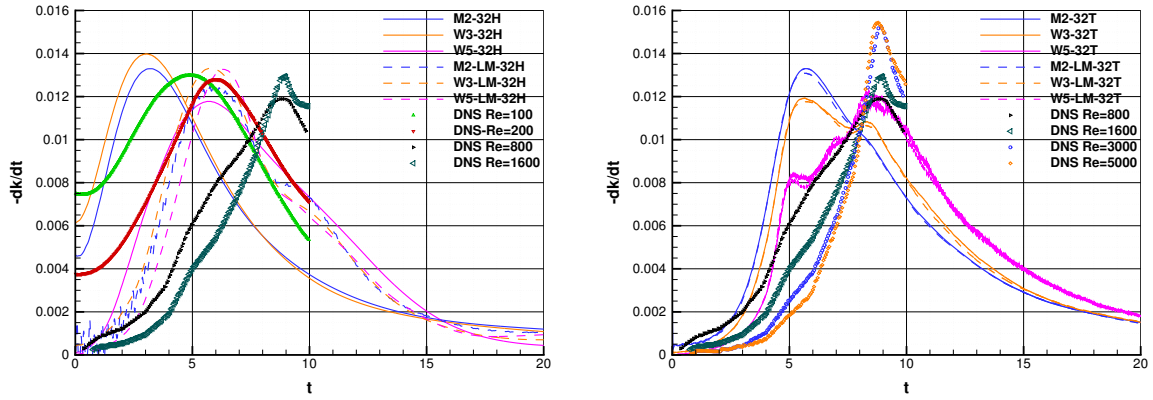

(a) Hexahedral 32H (b) Tetrahedral 32T

Figure 27: Total kinetic energy dissipation rate dK/dt temporal evolution for various schemes, grid resolutions, and LM treatment for the 3D Taylor-Green vortex test problem, and comparison with the DNS reference solutions of [71].

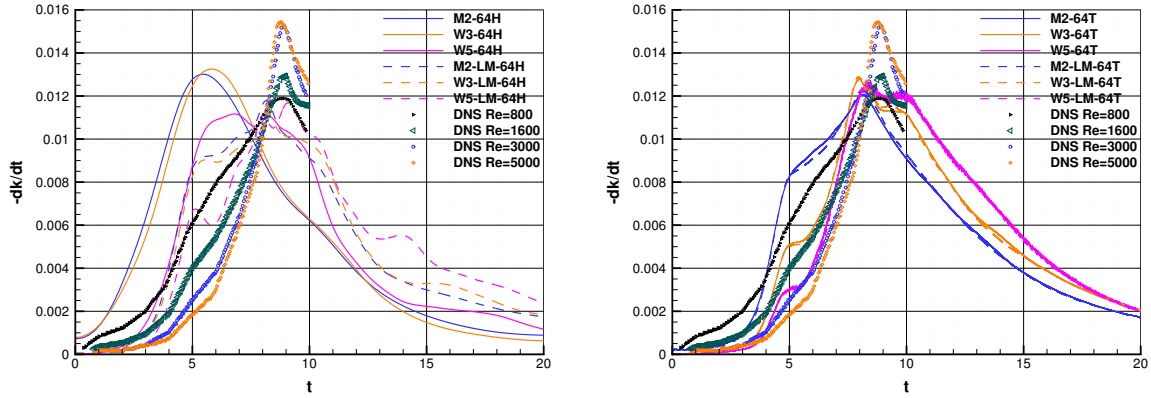

(a) Hexahedral 64H (b) Tetrahedral 64T

Figure 28: Total kinetic energy dissipation rate dK/dt temporal evolution for various schemes, grid resolutions, and LM treatment for the 3D Taylor-Green vortex test problem, and comparison with the DNS reference solutions of [71].

In Fig. 29 and Fig. 30, the conservation error in terms total kinetic energy for all the schemes is plotted with respect to number of cells and CPU time respectively. In the incompressible limit kinetic energy can only be damped by large scale viscous effects, either by explicit SGS models, or by the viscosity of the numerical scheme itself [65]. Therefore, this measure is used to evaluate the numerical dissipation effects of various schemes. The kinetic energy conservation error presented in Fig. 29 demonstrates lower error for the tetrahedral meshes than the hexahedral meshes with respect to the number of cells without the LM treatment. The situation is significantly altered when the LM treatment is used, since the hexahedral meshes with the LM treatment provide smaller errors than the tetrahedral meshes for similar number of cells as shown in Fig. 29. This pattern is repeated for the variation of error with respect to CPU time as shown in Fig. 30. A negative impact on the performance of the WENO 5^{th}-order scheme can be noticed for the LM treatment on the coarsest tetrahedral mesh which is assumed to be related to the dispersive errors present.

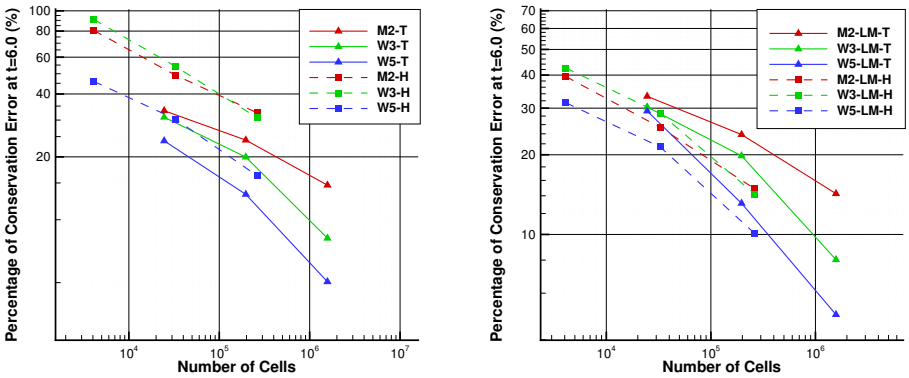

(a) without LM treatment (b) with LM treatment

Figure 29: Conservation error at $t = 6$ in terms of total kinetic energy and number of cells for various schemes, grid resolutions, and LM treatment for the 3D Taylor-Green vortex test problem.

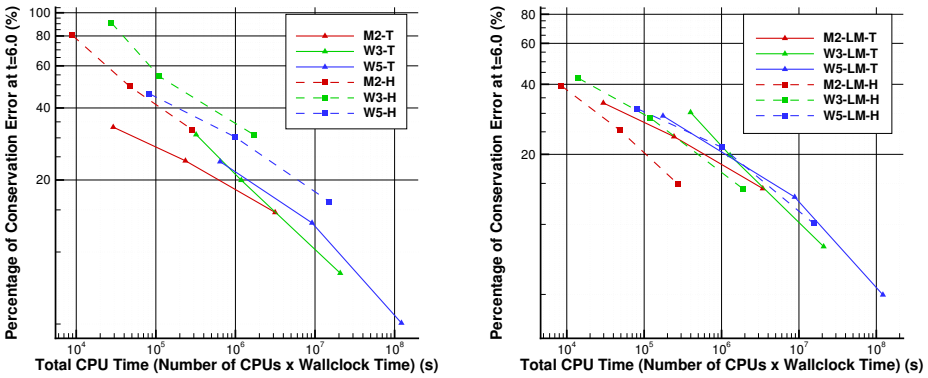

(a) without LM treatment

(b) with LM treatment

Figure 30: Conservation error at $t = 6$ in terms of total kinetic energy and CPU time (Number of CPUs x Wallclock Time in seconds) for various schemes, grid resolutions, and LM treatment for the 3D Taylor-Green vortex test problem.

The LM treatment provides significant improvement in terms of the error measure for hexahedral cells. The CPU time taken for a WENO 3^{th}-order scheme with the LM treatment is at least one order of magnitude smaller than a WENO 5^{th}-order scheme without LM treatment as shown in Fig.30 for the similar error. The primary reason for that is that the jump between the intercell states is larger for the 5^{th}-order scheme therefore the impact of this treatment is more prominent. Therefore, savings in terms of CPU time can be expected using this LM treatment, since lower-order methods can be utilised and provide accuracy equivalent to a more costly higher-order scheme. On the other hand the LM treatment does not offer any significant benefits for the tetrahedral meshes, although it does not degrade their performance as also documented by Rieper [45], but it did not produce the inaccurate results of the original treatment as experienced by Rieper [45].

3.5. SD7003 Aerofoil

The last test-case showcases the improvements of the LM treatment for hybrid unstructured grids for engineering applications. The test cases concerns the turbulent flow over the SD7003 wing at Mach number of $M = 0.2$, angle of attack of $\alpha = 8°$ and Reynolds number $Re = 60,000$ based on the chord length. This flow is characterised by a laminar separation region, which reattaches further downstream forming a Laminar Separation Bubble (LSB), and along the separation bubble transition to turbulence occurs. This test case is widely used to document the performance of various numerical schemes in the context of LES, for predicting separation, transition and turbulent flow [14,24 ,72 ,73].

For this case a hybrid unstructured mesh of approximately 5.6 million cells is generated, consisting of hexahedral and prismatic cells as illustrated in Fig.31 . The domain extends $20c$ upstream and downstream, and $0.2c$ in the span-wise direction, where c is the chord length. The grid resolution at the boundary layer region gives a $y^+ \approx 1$ at the first cell off the surface, 80 cells are used in the span-wise direction, 400 and 150 cells are used for the upper and lower part of the aerofoil, and 42 layers are extruded in the direction normal to the surface with an expansion factor of 1.035. The leading edge and trailing edge grid spacings correspond to $x^+ \approx 2$ with an expansion factor 1.035, and in the span-wise direction a $z^+ \approx 84$ is used. Periodic boundary conditions are used in the span-wise direction, no-slip boundary conditions at the surface of the aerofoil and free-stream conditions at the farfield. The WENO 4^{th}-order schemes is employed, a CFL number of 0.9 is set along with the explicit Runge-Kutta 3rd-order scheme, that results in time step size of $\Delta t \approx (10^{-4})t_c$, where $t_c = c/U_\infty$. The simulations were run for $t = 20t_c$ to develop the flow, and an additional $20t_c$ for time averaging.

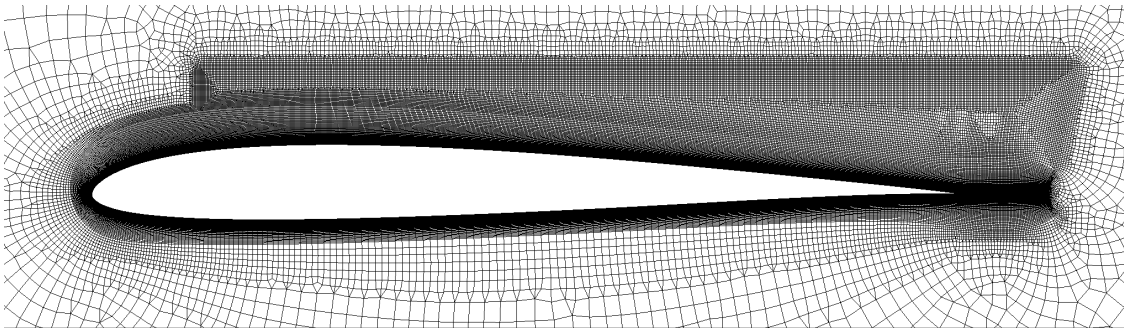

Figure 31: Slice of the mesh used for the SD7003 test problem.

Contours of time and span-averaged streamwise velocity are shown in Fig. 32, where it can be noticed that the laminar separation bubble near the leading edge on the suction side of the aerofoil, is smaller for the with the LM treatment compared without the LM treatment. The separation and reattachment positions are in better agreement with the reference data sets [24, 72, 73] when the LM treatment is employed as it shown in Table 3. Without engaging the LM treatment, the reattachment position is predicted further downstream, worsening the agreement with the reference data.

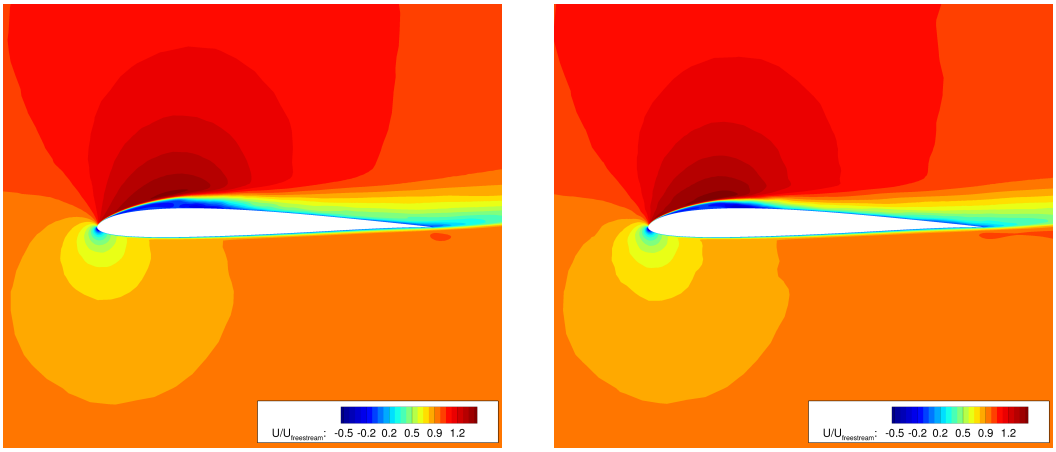

(a) without LM treatment (b) with LM treatment

Figure 32: Span-averaged and time-averaged stream-wise velocity contour for the SD7003 test problem using WENO 4^{th}-order schemes.

The instantaneous isosurfaces of q-criterion colored by the velocity magnitude are shown in Fig. 33 for the fully developed flow after $20t_c$. Smaller flow structures seem to be captured by the numerical schemes with the LM fix, which is inline with findings from the Taylor-Green vortex flow, where a decreased dissipation is observed for hexahedral dominant meshes.

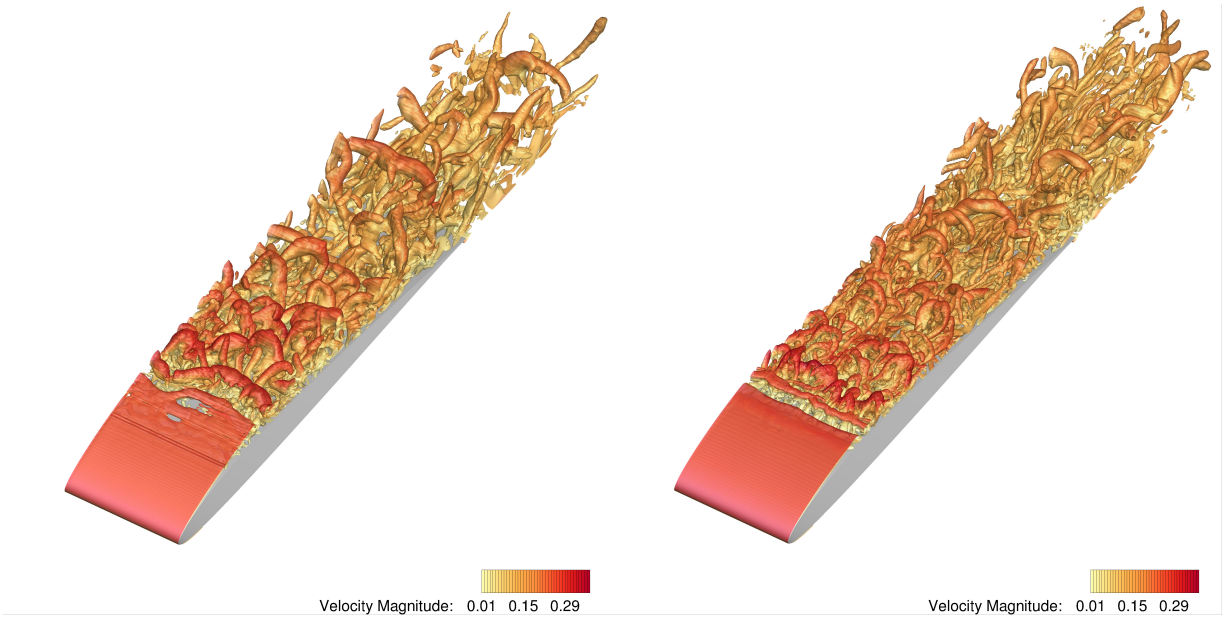

(a) without LM treatment (b) with LM treatment

Figure 33: Instantaneous isosurfaces of Q criterion coloured by velocity magnitude for the SD7003 test problem using WENO 4^{th}-order schemes.

The span-averaged and time-averaged pressure coefficient C_P distribution is plotted in Fig. 34, along with the reference data sets [24, 72, 73]. When the LM treatment is enabled the results are in closer agreement with the reference data sets in particular with the ones of Beck et al. [73],including the location of the transition region, where without it the transition appears further downstream. The LM treatment improves the results for the present test problem for all the parameters investigated, including pressure distribution and range of turbulent scales resolved. This is achieved without any significant increase in cost since the treatment is compact, local and inexpensive, highlighting that the results of compressible flow simulations can experience significant improvements in low Mach regions of the flow, even for higher-order numerical schemes.

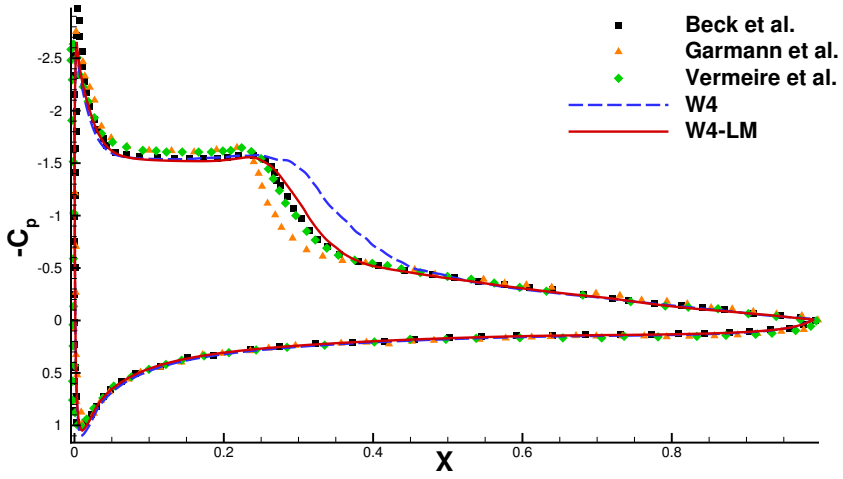

Figure 34: Span-averaged and time-averaged pressure coefficient C_P distribution along the chord of the SD7003 aerofoil, using WENO 4th-order schemes and comparison with reference datasets from Garmann et al. [72], Vermeire et al. [24] and Beck et al. [73]

Table 3: Obtained results for the SD7003 test cases using WENO 4th-order schemes, and comparison with reference datasets.

Data set	C_L	C_D	x_{sep}/c	x_{rea}/c	Method
Present W4	0.903	0.058	0.038	0.391	4th-order WENO FV
Present W4-LM	0.928	0.051	0.029	0.329	4th-order WENO FV
Garmann et al. [72]	0.969	0.039	0.023	0.259	6th-order FD
Vermeire et al. [24]	0.941	0.049	0.045	0.315	5th-order FR
Beck et al. [73]	0.932	0.050	0.030	0.336	8th-order DG

4. Conclusions

In this work, a low-Mach number treatment is presented based on the original formulation of Thornber et al. [31] and the revised one by Oßwald et al. [39]. When directly applying the original formulation of Thornber et al. [31] to unstructured, multidimensional FV schemes inaccurate results were obtained. The revised formulation based on the approach of Oßwald et al. [39] only modifies the velocities in the normal direction of the intercell states, since the tangential velocities need more dissipation according to Thornber et al. [31] and can be used with any Riemann solver. This treatment has been applied to a series of test problems including the subsonic and supersonic flow past a cylinder, the 2D vortex evolution, the 3D Taylor-Green vortex, and the turbulent flow past the SD7003 aerofoil on meshes consisting of various element types.

The obtained results indicate that the LM treatment can actually improve the dissipation characteristics of the schemes, especially at low-Mach number flow regions in the presence of quadrilateral and hexahedral elements. However, for triangular and tetrahedral elements the use of this treatment does not provide as significant benefits as for other element types. Some combinations of numerical schemes and grid resolutions for these elements are characterised by dispersion errors and a further investigation of this mechanism is underway for future studies. However, the LM treatment can provide significant benefits in CPU time in the sense that a lower-order method can be used and provide equivalent results with a higher-order method without the treatment particularly for quadrilateral and hexahedral elements, that are usually employed close to the boundary layer region.

The main goal of this treatment is not to simulate with great accuracy very low-Mach number flows, where the use of the incompressible equations would be more appropriate, but to improve the resolution

of the schemes at low-Mach number regions that are present in compressible flow simulations that can include regions of sharp and smooth flow gradients. It has to be stressed that the majority of the LM treatments take into account only the local-Mach number, in order to modify the variables accordingly, however other parameters such as the dissipation and dispersion properties in conjunction with the local grid-resolution should also be taken into account since it was found that different types of meshes show different sensitivity in these treatments. For turbulent flow simulations these low-Mach number regions are close to the boundary layer are most often discretised by hexahedral or prismatic elements. This LM treatment resulted in improvements in resolving these low-Mach regions of turbulent flows accurately in the SD7003 aerofoil test problem, and it indicates that it can benefit higher-order schemes as well. Finally the compact, simple and inexpensive nature of this treatment makes it an appealing candidate solution to be implemented in various compressible CFD codes.

Acknowledgements

The authors would like to thank Jaguar Land Rover for granting permission to publish this work. The work has been undertaken due to funding from EPSRC Award. Ref. Number: 13794. The authors acknowledge the computing time on the UK national high-performance computing service ARCHER that was provided through the UK Turbulence Consortium in the framework of the EPSRC grant EP/L000261/1. Panagiotis Tsoutsanis acknowledges the computing time at HAZELHEN at the High-Performance Computing Center Stuttgart (HLRS), Germany and SuperMUC at the Leibniz Supercomputing Centre (LRZ) in Garching, Germany in the framework of the PRACE project funded in part by the EU Horizon 2020 research and innovation programme (2014-2020) under grant agreement 653838. The authors would also like to acknowledge the constructive comments, and suggestions provided by the anonymous reviewers that greatly improved the quality of the article.

References

[1] M. Dumbser, M. Kaser, V. Titarev, E. Toro, Quadrature-free non-oscillatory finite volume schemes on unstructured meshes for nonlinear hyperbolic systems, Journal of Computational Physics 226 (1) (2007) 204–243.

[2] M. Dumbser, D. Balsara, E. Toro, C.-D. Munz, A unified framework for the construction of one-step finite volume and discontinuous Galerkin schemes on unstructured meshes, Journal of Computational Physics 227 (18) (2008) 8209–8253.

[3] A. Haselbacher, A WENO reconstruction algorithm for unstructured grids based on explicit stencil construction, 2005, pp. 3369–3378.

[4] W. Li, Y. Ren, Quadrature-free non-oscillation finite volume scheme for solving Navier-Stokes equations on unstructured grids, Vol. 1376, 2011, pp. 639–641.

[5] X. Nogueira, L. Cueto-Felgueroso, I. Colominas, F. Navarrina, M. Casteleiro, A new shock-capturing technique based on moving least squares for higher-order numerical schemes on unstructured grids, Computer Methods in Applied Mechanics and Engineering 199 (37-40) (2010) 2544–2558.

[6] C. Ollivier-Gooch, Quasi-ENO schemes for unstructured meshes based on unlimited data-dependent least-squares reconstruction, Journal of Computational Physics 133 (1) (1997) 6–17.

[7] C. O. Gooch, M. V. Altena, A high-order-accurate unstructured mesh finite-volume scheme for the advection-diffusion equation, Journal of Computational Physics 181 (2) (2002) 729–752.

[8] P. Tsoutsanis, V. Titarev, D. Drikakis, WENO schemes on arbitrary mixed-element unstructured meshes in three space dimensions, Journal of Computational Physics 230 (4) (2011) 1585–1601.

[9] V. Titarev, P. Tsoutsanis, D. Drikakis, WENO schemes for mixed-element unstructured meshes, Communications in Computational Physics 8 (3) (2010) 585–609.

[10] W. Wolf, J. Azevedo, High-order ENO and WENO schemes for unstructured grids, International Journal for Numerical Methods in Fluids 55 (10) (2007) 917–943.

[11] Z. Xu, Y. Liu, C.-W. Shu, Hierarchical reconstruction for discontinuous Galerkin methods on unstructured grids with a WENO-type linear reconstruction and partial neighboring cells, Journal of Computational Physics 228 (6) (2009) 2194–2212.

[12] Z. Xu, Y. Liu, C.-W. Shu, Hierarchical reconstruction for spectral volume method on unstructured grids, Journal of Computational Physics 228 (16) (2009) 5787–5802.

[13] P. Tsoutsanis, A. Antoniadis, D. Drikakis, WENO schemes on arbitrary unstructured meshes for laminar, transitional and turbulent flows, Journal of Computational Physics 256 (2014) 254–276.

[14] B. Vermeire, P. Vincent, On the properties of energy stable flux reconstruction schemes for implicit large eddy simulation, Journal of Computational Physics 327 (2016) 368–388.

[15] B. Cockburn, C.-W. Shu, Runge-Kutta discontinuous Galerkin methods for convection-dominated problems, Journal of Scientific Computing 16 (3) (2001) 173–261.
[16] J. Dennis, R. Nair, H. Tufo, M. Levy, T. Voran, Development of a scalable global discontinuous Galerkin atmospheric model, Int. J. Comp. Sci. Eng.
[17] A. Uranga, P.-O. Persson, M. Drela, J. Peraire, Implicit large eddy simulation of transition to turbulence at low Reynolds numbers using a discontinuous Galerkin method, International Journal for Numerical Methods in Engineering 87 (1-5) (2011) 232–261.
[18] J. Zhu, J. Qiu, C.-W. Shu, M. Dumbser, Runge-Kutta discontinuous Galerkin method using WENO limiters ii: Unstructured meshes, Journal of Computational Physics 227 (9) (2008) 4330–4353.
[19] Z. Wang, Spectral (finite) volume method for conservation laws on unstructured grids. basic formulation, Journal of Computational Physics 178 (1) (2002) 210–251.
[20] Z. Wang, Y. Liu, Spectral (finite) volume method for conservation laws on unstructured grids. ii. extension to two-dimensional scalar equation, Journal of Computational Physics 179 (2) (2002) 665–697.
[21] Z. Wang, L. Zhang, Y. Liu, Spectral (finite) volume method for conservation laws on unstructured grids iv: Extension to two-dimensional systems, Journal of Computational Physics 194 (2) (2004) 716–741.
[22] Y. Zhou, Z. Wang, Implicit large eddy simulation of transitional flow over a SD7003 wing using high-order spectral difference method, 2010.
[23] C. Breviglieri, A. Maximiliano, E. Basso, J. Azevedo, Improved high-order spectral finite volume method implementation for aerodynamic flows, 2009.
[24] B. Vermeire, F. Witherden, P. Vincent, On the utility of gpu accelerated high-order methods for unsteady flow simulations: A comparison with industry-standard tools, Journal of Computational Physics 334 (2017) 497–521.
[25] R. Abgrall, On essentially non-oscillatory schemes on unstructured meshes: analysis and implementation, Journal of Computational Physics 114 (1) (1994) 45–58.
[26] D. Stanescu, W. Habashi, Essentially nonoscillatory Euler solutions on unstructured meshes using extrapolation, AIAA Journal 36 (8) (1998) 1413–1416.
[27] G. S. Jiang, C. W. Shu, Efficient implementation of weighted ENO schemes, Journal of Computational Physics 126 (1) (1996) 202–228.
[28] J. Shi, C. Hu, C.-W. Shu, A technique of treating negative weights in WENO schemes, Journal of Computational Physics 175 (1) (2002) 108–127.
[29] C.-W. Shu, S. Osher, Efficient implementation of essentially non-oscillatory shock-capturing schemes, Journal of Computational Physics 77 (2) (1988) 439–471.
[30] O. Friedrich, Weighted essentially non-oscillatory schemes for the interpolation of mean values on unstructured grids, Journal of Computational Physics 144 (1) (1998) 194–212.
[31] B. Thornber, A. Mosedale, D. Drikakis, D. Youngs, R. Williams, An improved reconstruction method for compressible flows with low Mach number features, Journal of Computational Physics 227 (10) (2008) 4873–4894.
[32] X. Nogueira, L. RamÃrez, S. Khelladi, J.-C. Chassaing, I. Colominas, A high-order density-based finite volume method for the computation of all-speed flows, Computer Methods in Applied Mechanics and Engineering 298 (2016) 229–251.
[33] F. Qu, C. Yan, D. Sun, Z. Jiang, A new Roe-type scheme for all speeds, Computers and Fluids 121 (2015) 11–25.
[34] Z. Li, Y. Zhang, H. Chen, A low dissipation numerical scheme for implicit large eddy simulation, Computers and Fluids 117 (2015) 233–246.
[35] S. Matsuyama, Performance of all-speed ausm-family schemes for DNS of low Mach number turbulent channel flow, Computers and Fluids 91 (2014) 130–143.
[36] S. Shanmuganathan, D. Youngs, J. Griffond, B. Thornber, R. Williams, Accuracy of high-order density-based compressible methods in low Mach vortical flows, International Journal for Numerical Methods in Fluids 74 (5) (2014) 335–358.
[37] Y. Liu, M. Sun, Accuracy improvement of axisymmetric bubble dynamics using low Mach number scaling, Computers and Fluids 90 (2014) 147–154.
[38] X.-S. Li, C.-W. Gu, Mechanism of Roe-type schemes for all-speed flows and its application, Computers and Fluids 86 (2013) 56–70.
[39] K. Oswald, A. Siegmund, P. Birken, V. Hannemann, A. Meister, L2roe: A low dissipation version of Roe's approximate Riemann solver for low Mach numbers, International Journal for Numerical Methods in Fluids 81 (2) (2016) 71–86.
[40] Y. Shen, G. Zha, Low diffusion e-cusp scheme with implicit high order WENO scheme for preconditioned Navier-Stokes equations, Computers and Fluids 55 (2012) 13–23.
[41] F. Rieper, A low-Mach number fix for Roe's approximate Riemann solver, Journal of Computational Physics 230 (13) (2011) 5263–5287.
[42] F. Rieper, On the dissipation mechanism of upwind-schemes in the low Mach number regime: A comparison between Roe and HLL, Journal of Computational Physics 229 (2) (2010) 221–232.
[43] P. Roe, Approximate riemann solvers, parameter vectors, and difference schemes, Journal of Computational Physics 43 (2) (1981) 357–372. doi:10.1016/0021-9991(81)90128-5.
[44] F. Bassi, C. De Bartolo, R. Hartmann, A. Nigro, A discontinuous Galerkin method for inviscid low Mach number flows, Journal of Computational Physics 228 (11) (2009) 3996–4011.
[45] F. Rieper, G. Bader, The influence of cell geometry on the accuracy of upwind schemes in the low Mach number regime, Journal of Computational Physics 228 (8) (2009) 2918–2933.
[46] P. Tsoutsanis, I. Kokkinakis, L. Konozsy, D. Drikakis, R. Williams, D. Youngs, An investigation of the accuracy and efficiency of structured and unstructured, compressible and incompressible methods for the vortex pairing problem, Computer Methods in Applied Mechanics and Engineering 293 (2015) 207–231.

[47] A. F. Antoniadis, P. Tsoutsanis, D. Drikakis, Numerical accuracy in RANS computations of high-lift multi-element airfoil and aircraft configurations, in: AIAA (Ed.), 53rd AIAA Aerospace Sciences Meeting, no. AIAA 2015-0317, Kissimmee, Florida, 2015.
[48] D. Drikakis, A. F. Antoniadis, P. Tsoutsanis, I. Kokkinakis, Z. Rana, Azure: An advanced cfd software suite based on high-resolution and high-order methods, in: AIAA (Ed.), 53rd AIAA Aerospace Sciences Meeting, no. AIAA 2015-0813, Kissimmee, Florida, 2015.
[49] A. F. Antoniadis, D. Drikakis, I. Kokkinakis, P. Tsoutsanis, Z. Rana, High-order methods for hypersonic shock wave turbulent boundary layer interaction flow, in: AIAA (Ed.), 20th AIAA International Space Planes and Hypersonic Systems and Technologies Conference, no. AIAA 2015-3524, Glasgow, Scotland, 2015.
[50] A. Antoniadis, P. Tsoutsanis, D. Drikakis, Assessment of high-order finite volume methods on unstructured meshes for rans solutions of aeronautical configurations, Computers and Fluids 146 (2017) 86–104.
[51] P. Tsoutsanis, Extended bounds limiter for high-order finite-volume schemes on unstructured meshes, Journal of Computational Physics 362 (2018) 69–94.
[52] P. Tsoutsanis, A. Antoniadis, J. K.W., Improvement of the computational performance of a parallel unstructured WENO finite volume CFD code for Implicit Large Eddy Simulation, Computer and Fluids article (2018) in press. doi:doi.org/10.1016/j.compfluid.2018.03.012.
[53] P. Tsoutsanis, D. Drikakis, A high-order finite-volume method for atmospheric flows on unstructured grids, Journal of Coupled Systems and Multiscale Dynamics 4 (3) (2016) 170–186.
[54] M. Dumbser, M. Käser, V. A. Titarev, E. F. Toro, Quadrature-free non-oscillatory finite volume schemes on unstructured meshes for nonlinear hyperbolic systems, Journal of Computational Physics 226 (1) (2007) 204–243.
[55] T. J. Barth, D. C. Jespersen, The design and application of upwind schemes on unstructured meshes, 27th Aerospace Sciences Meeting.
[56] E. Toro, M. Spruce, W. Speares, Restoration of the contact surface in the hll-riemann solver, Shock Waves 4 (1) (1994) 25–34.
[57] L. Ivan, C. Groth, High-order solution-adaptive central essentially non-oscillatory (ceno) method for viscous flows, Journal of Computational Physics 257 (PA) (2014) 830–862. doi:10.1016/j.jcp.2013.09.045.
[58] G. Gassner, F. Lorcher, C.-D. Munz, A contribution to the construction of diffusion fluxes for finite volume and discontinuous galerkin schemes, Journal of Computational Physics 224 (2) (2007) 1049–1063.
[59] A. Jalali, M. Sharbatdar, C. Ollivier-Gooch, Accuracy analysis of unstructured finite volume discretization schemes for diffusive fluxes, Computer and Fluids 101 (2014) 220–232.
[60] H. Nishikawa, Robust and accurate viscous discretisation via upwind scheme-i: Basic principle, Computer and Fluids 49 (2011) 62–86.
[61] S. Gottlieb, On high order strong stability preserving Runge-Kutta and multi step discretizations, Journal of Scientific Computing 25 (112) (2005) 105–128.
[62] I. Kokkinakis, D. Drikakis, Implicit large eddy simulation of weakly-compressible turbulent channel flow, Computer Methods in Applied Mechanics and Engineering 287 (2015) 229–261.
[63] A. V. Rodionov, Artificial viscosity in Godunov-type schemes to cure the carbuncle phenomenon, Journal of Computational Physics 345 (2017) 308–329.
[64] V. Rusanov, Calculation of interaction of non-steady shock waves with obstacles, J Comput Math Phys USSR 1 (1961) 267â79.
[65] D. Drikakis, C. Fureby, F. Grinstein, D. Youngs, Simulation of transition and turbulence decay in the Taylor-Green vortex, Journal of Turbulence 8 (2007) 1–12.
[66] J. Bull, A. Jameson, Simulation of the Taylor-Green vortex using high-order flux reconstruction schemes, AIAA Journal 53 (9) (2015) 2750–2761.
[67] M. Dumbser, I. Peshkov, E. Romenski, O. Zanotti, High order ADER schemes for a unified first order hyperbolic formulation of continuum mechanics: Viscous heat-conducting fluids and elastic solids, Journal of Computational Physics 314 (2016) 824–862.
[68] J.-B. Chapelier, M. de la Llave Plata, E. Lamballais, Development of a multiscale LES model in the context of a modal discontinuous Galerkin method, Computer Methods in Applied Mechanics and Engineering 307 (2016) 275–299.
[69] A. Sifounakis, S. Lee, D. You, A conservative finite volume method for incompressible Navier-Stokes equations on locally refined nested cartesian grids, Journal of Computational Physics 326 (2016) 845–861.
[70] C.-W. Shu, W.-S. Don, D. Gottlieb, O. Schilling, L. Jameson, Numerical convergence study of nearly incompressible, inviscid Taylor-Green vortex flow, Journal of Scientific Computing 24 (1) (2005) 569–595.
[71] M. Brachet, D. Meiron, B. Nickel, R. Morf, U. Frisch, S. Orszag, Small-scale structure of the Taylor-Green vortex, Journal of Fluid Mechanics 130 (1983) 411–452.
[72] D. Garmann, M. Visbal, P. Orkwis, Comparative study of implicit and subgrid-scale model large-eddy simulation techniques for low-reynolds number airfoil applications, International Journal for Numerical Methods in Fluids 71 (12) (2013) 1546–1565.
[73] A. Beck, T. Bolemann, D. Flad, H. Frank, G. Gassner, F. Hindenlang, C.-D. Munz, High-order discontinuous galerkin spectral element methods for transitional and turbulent flow simulations, International Journal for Numerical Methods in Fluids 76 (8) (2014) 522–548.